Julia Eichberger

Model-based T_1 Quantification Methods and their Acceleration Potential for the Variable Flip Angle Approach

Master Thesis

Institute for Medical Engineering
Technical University of Graz
Stremayrgasse 16/III
A-8010 Graz
Head of the Institute: Univ.-Prof. Dr.techn. Dipl.-Ing. Rudolf Stollberger

Advisor: Dipl.-Ing. Oliver Maier
Reviewer: Univ.-Prof. Dipl.-Ing. Dr.techn. Rudolf Stollberger

Graz, September 9, 2019

Statutory Declaration

I declare that I have authored this thesis independently, that I have not used other than the declared sources / resources, and that I have explicitly marked all material which has been quoted either literally or by content from the used sources.

Eidesstattliche Erklärung

Ich erkläre an Eides statt, dass ich die vorliegende Arbeit selbstständig verfasst, andere als die angegebenen Quellen/Hilfsmittel nicht benutzt und die den benutzten Quellen wörtlich und inhaltlich entnommene Stellen als solche kenntlich gemacht habe.

Ort	Datum	Unterschrift

Acknowledgements

First of all I would like to express my gratitude to Prof. Rudolf Stollberger for supervising this master thesis, and steering it in the right direction.

A special thank you goes to my advisors Oliver Maier and Matthias Schlögel for introducing me to the subject and guiding me throughout the project with their expertise.

Finally I would like to thank my parents Renate and Dietmar and my husband Fabian for their support and encouragement throughout my years of study and especially during the process of researching and writing this thesis.

Abstract

Quantitative Magnetic Resonance Imaging (qMRI) techniques aim at generating images with absolute values independent of the used measurement protocol. Most T_1 quantification methods suffer from long acquisition times and methods allowing for faster T_1 mapping are subject of current research. Model-based Reconstruction (MBR) is a promising method in terms of scan time reduction and accuracy of fit. The present work analyzes model-based T_1 quantification methods based on the Variable Flip Angle (VFA) model in terms of their stability to different scanning scenarios, focusing especially on their acceleration potential. Working on either image or k-space data an Iterative Regularized Gauss-Newton (IRGN)-framework is used for the solution of the problem. T_1 estimates are in overall good agreement with reference values for numerical phantom and in vivo data. Superiority of TGV^2_{frob} regularization to other regularization functionals is shown in numerical simulations and Acceleration Factors (AFs) up to 19.7 are achieved using the proposed IRGN-TGV^2_{frob} reconstruction on in vivo data. The inclusion of other signal models could be subject of further investigation.

Kurzfassung

Quantitative Magnetresonanztomographie (qMRT) zielt auf die Gewinnung von Bildern mit absoluten Werten unabhängig vom verwendeten Messprotokoll ab. Die meisten Methoden zur T_1-Quantifizierung gehen mit langen Aquisitionszeiten einher und Methoden die ein schnelleres T_1-Mapping ermöglichen sind Gegenstand aktueller Forschung. Modellbasierte Rekonstruktion (MBR) ist eine vielversprechende Methode in Bezug auf die Reduzierung der Scan-Zeit sowie die Genauigkeit von T_1. Die vorliegende Arbeit analysiert modellbasierte T_1-Quantifizierungsmethoden basierend auf dem VFA-Modell hinsichtlich ihrer Stabilität unter verschiedenen Mess-Bedingungen, wobei der Schwerpunkt insbesondere auf ihrem Beschleunigungpotenzial liegt. Die Rekonstruktion ist sowohl von Bild- als auch k-Raum-Daten möglich, zur Lösung des Rekonstruktionsproblems wird ein IRGN-Framework verwendet. Die T_1-Werte stimmen insgesamt gut mit den Referenzwerten überein, sowohl für das numerisches Phantom als auch für in vivo Daten. Die Überlegenheit der TGV_{frob}^2-Regularisierung gegenüber anderen Regularisierungsmethoden ist in den numerischen Simulationen ersichtlich und mit der IRGN-TGV_{frob}^2-Rekonstruktion werden Beschleunigungsfaktoren bis zu 19.7 bei der Rekonstruktion von in-vivo-Daten erzielt. Die Integration weiterer Signalmodelle könnte Gegenstand weiterer Untersuchungen sein.

Contents

1 Introduction **1**

1.1 Background 2

1.1.1 T_1 Relaxation 2

1.1.2 T_2 and T_2^* Relaxation 2

1.1.3 The Variable Flip Angle Approach 3

1.1.4 Model-based Reconstruction 6

1.1.5 Flip Angle Selection 7

1.1.6 Accelerated T_1 Mapping 9

1.2 Definition of Task 10

2 Methods **11**

2.1 Image-space Based T_1 Quantification 12

2.1.1 Algorithms 13

2.1.1.1 DESPOT 13

2.1.1.2 Model-based Reconstruction in Image-space 14

2.1.2 Flip Angle Determination 22

2.1.3 Flip Angle Verification 23

2.1.4 Statistical Evaluation 24

2.2 Accelerated Variable Flip Angle T_1 Quantification 24

2.2.1 Model-based Reconstruction in k-Space 24

2.2.2 ICTGV reconstruction and Model-based Reconstruction in Image-space 26

2.2.3 Bloch-Siegert B_1^+ Mapping and Coil Calibration 26
2.2.4 Data Acquisition 29
2.2.4.1 Radial Volumetric Encoding Sequence 30
2.2.5 ROI-based Evaluation 32

3 Results 34

3.1 Numerical Simulation 34
3.1.1 Flip Angle Selection 34
3.1.2 Robustness to SNR Level 35
3.1.3 Accelerated T_1 Mapping 41
3.2 In Vivo Brain Measurements 43
3.2.1 SNR Stability 46
3.2.2 Accelerated T_1 Mapping 46
3.2.2.1 Model-based Reconstruction in k-Space 57

4 Discussion and Conclusion 63

4.1 Numerical Simulations 63
4.2 In Vivo Reconstruction 65
4.2.1 SNR Stability 65
4.2.2 Comparison of Mapping Methods 66
4.2.3 Acceleration Potential 67
4.3 Conclusion 68

5 Algorithms 70

Abbreviations

T_A	Acquisition Time
T_E	Echo Time
T_I	Inversion Time
T_R	Repetition Time
AF	Acceleration Factor
CG	Conjugate Gradient
CN	Caudate Nucleus
CSF	Cerebrospinal Fluid
DESPOT	Driven Equilibrium Single Pulse Observation of T_1
FA	Flip Angle
FLASH	Fast Low Angle Shot
FOV	Field of View
GA	Golden Angle
GM	Gray Matter

GN	Gauss-Newton
ICTGV	Infimal Convolution Total Generalized Variation
IR	Inversion Recovery
IRGN	Iterative Regularized Gauss-Newton
MBR	Model-based Reconstruction
MRF	Magnetic Resonance Fingerprinting
MRI	Magnetic Resonance Imaging
MR	Magnetic Resonance
P	Putamen
PD	Proton Density
PI	Parallel Imaging
RAVE	Radial Volumetric Encoding
RF	Radio Frequency
ROI	Region of Interest
SAR	Specific Absorption Rate
SENSE	Sensitivity Encoding
SNR	Signal to Noise Ratio
SOS	Sum of Squares

SPF	Spokes per Frame
SPGR	Spoiled Gradient Echo
TGV	Total Generalized Variation
TV	Total Variation
VFA	Variable Flip Angle
WM	White Matter

1 Introduction

Magnetic Resonance Imaging (MRI) is an imaging modality know especially for its good soft tissue contrast, its non-invasivness, and its functionality without radiation. Since its first days it has overcome many challenges, including long scan times as well as low Signal to Noise Ratio (SNR) which lead to poor image resolution. Many improvements have been developed since then, making MRI a vital tool for clinical routine diagnostic. The possibility to acquire different image contrast, depending on the clinical question at hand, played a major role in the success story of MRI. However, the ability to change the signal intensity of a specific tissue and therefore the image contrast also has its drawback. Since the signal intensity does not solely depend on the physical parameters of the tissue, no general assumption about physical properties can be derived from the simple images.

To enhance contrast in an Magnetic Resonance (MR) image, scanning parameters are chosen in a way that the physical parameter promising best contrast in the observed region contributes most to the signal. The resultant image is then said to be weighted in this specific parameter. For example the image is termed T_1 weighted, if differences in the longitudinal relaxation time T_1 contribute most to its contrast. However, other tissue parameters still contribute to the overall contrast. An insight to the sensitivity of the image contrast to the setting of the timing parameters (Repetition Time (T_R), Echo Time (T_E) and the Flip Angle (FA) α) will be given later in this work, when analysing the signal equation of the used Fast Low Angle Shot (FLASH) Sequence.

Quantitative MRI techniques aim at generating images with absolute values independent of the used measurement protocol. Longitudinal and transverse relaxation times, T_1 and T_2 respectively, as well as the Proton Density (PD) ρ represent possible quantities for parameter mapping. These tissue parameters can be expected to be reproducible, and therefore quantitative, for a given scan configuration determined by e.g. field strength and temperature. Most T_1 quantification methods, including the current gold standard for T_1 parameter mapping, an Inversion Recovery (IR) spin echo sequence, suffer from long Acquisition Times (T_As) compared to qualitative T_1-weighted imaging. As time is a crucial factor in the clinical environment, the development of methods allowing for faster T_1 mapping are subject of current research.

1.1 Background

1.1.1 T_1 Relaxation

After the spin System is perturbed by a Radio Frequency (RF) pulse at the Larmor frequency, the longitudinal magnetization M_z recovers to its equilibrium value M_0. This recovery known as T_1 or longitudinal relaxation is caused by energy transfer from the spins to their environment and is therefore also called spin-lattice relaxation. The eponymous time constant T_1 corresponds to the time needed by M_z to regain 63% of its maximum value M_0 after fully excitation with a 90 degree RF pulse. T_1 relaxation additionally depens on the molecular motion and the used field strength and follows a mono-exponential function, described by $M_z = M_0 \left(1 - exp\left(-\frac{t}{T_1}\right)\right)$.

1.1.2 T_2 and T_2^* Relaxation

Occuring parallel to and independent from T_1 relaxation another relaxation process, caused by spin-spin interactions and accounting for loss of transverse magnetization M_{xy}, takes place. The underlying phenomenon for this transverse relaxation are small fluctuations of the local magnetic field caused by neighboring spins, consequently leading to their dephasing and making them loose their initial coherence. T_2 relaxation like T_1 relaxation follows a mono-exponential function, described by $M_{xy} = M_0\, exp\left(-\frac{t}{T_2}\right)$, with T_2 being the time after which the transverse magnetization M_{xy} has been reduced to 37% of its initial value. Field inhomogeneities account for additional dephasing leading to an even faster signal decay with a time constant T_2^*.

1.1.3 The Variable Flip Angle Approach

The VFA approach is a method to determine T_1 maps. It is based on the FLASH sequence and a variation of its flip angle α. FLASH is a Spoiled Gradient Echo (SPGR) sequence, described by:

$$S_{FLASH} = \frac{M_0 \sin(\alpha)\,(1 - E_1)}{1 - E_1 \cos(\alpha)} E_2 \tag{1.1}$$

where $E_1 = e^{\frac{-T_R}{T_1}}$ and $E_2 = e^{\frac{-T_E}{T_2^*}}$ describe the longitudinal and transversal relaxation rates.

The signal intensity S_{FLASH} is a function of T_1, T_R, the flip angle α and a factor M_0, which is a quantity proportional to the equilibrium longitudinal magnetization. Figure 1.1 shows the corresponding sequence diagram, figure 1.2 the signal intensity of a FLASH sequence in dependence of α and T_1.

The contrast behaviour of the FLASH Sequence for different scanning parameters can be easily derived by looking at the corresponding signal equation 1.1. The T_2^*-weighting can be controlled by choice of echo time T_E, with a short T_E accounting for a small T_2^*-contribution. The T_1-weighting depends on the choice of the repetition time T_R as

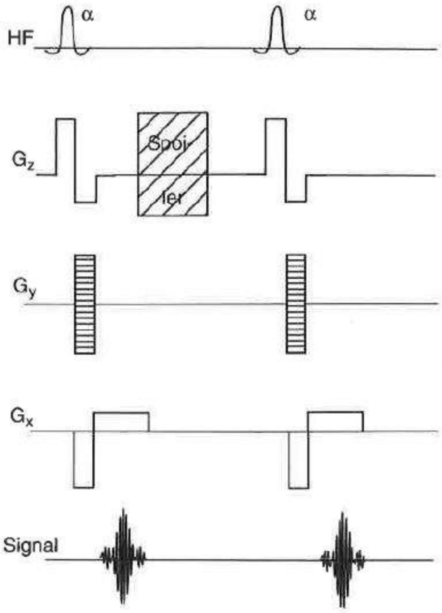

Figure 1.1: FLASH Sequence diagram. Figure taken from [1].

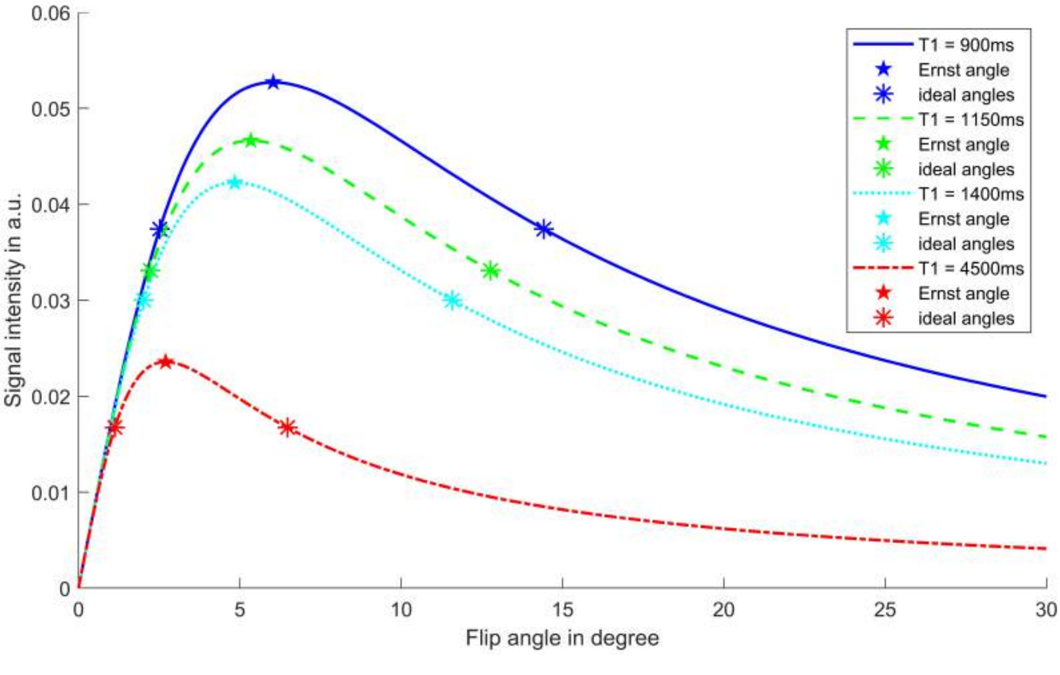

Figure 1.2: Signal intensity of the FLASH sequence over a range of flip angles, for different T_1 values and a constant T_R of 5ms, shows the dependency on this parameters. A pentagram denotes the Ernst angle, which maximizes the signal for a given T_R to T_1 ratio, the pair of asterisk shows the ideal dual angle set, according to Deoni et al.[2].

well as on the choice of the flip angle α. A short T_R in combination with a large flip angle α maximises the T_1-influence on the signal. However, for small flip angles $\cos(\alpha)$ approaches one and the terms $(1 - E_1)$ cancel, thereby removing the T_1-contribution to the signal. This leads to an image being either PD- or T_2^*-weighted, depending on the choice of T_E. Spoiling of any coherent transverse magnetization following each excitation pulse aims at eliminating the T_2-influence on the signal. Assuming ideal spoiling the E_2-term in equation 1.1 can be omitted, giving a signal equation that depends solely on the longitudinal relaxation time T_1. This simplification is further justified by choosing a short echo time T_E and keeping it constant. Any remaining T_2^* influence will lead to a variation of the proportionality constant M_0.

Omitting the E_2-term and linearizing equation 1.1 yields:

$$\frac{S_{FLASH}}{\sin(\alpha)} = \frac{S_{FLASH}}{\tan(\alpha)} E_1 + M_0 (1 - E_1) \tag{1.2}$$

which is of form $Y = Xm + b$, with m being the slope and b the intercept of the $\frac{S_{FLASH}}{\sin(\alpha)}$ over $\frac{S_{FLASH}}{\tan(\alpha)}$ signal curve. From m and b, T_1 and M_0 can be easily obtained, see 1.3a and 1.3b. This linearization is known as Driven Equilibrium Single Pulse Observation of T_1 (DESPOT) [2] in the literature. The linear relationship is only true in the high SNR regime and can lead to severe estimation errors of T_1 else.

$$T_1 = \frac{-T_R}{\ln(m)} \tag{1.3a}$$

$$M_0 = \frac{b}{1 - m} \tag{1.3b}$$

Potential error sources when using the VFA approach originate from assumptions like complete spoiling in-between excitations and perfect RF pulses. Especially with short T_R times and higher field strength this assumptions do not necessarily hold and their correction must be taken into account.

The transmit FA is known to deviate from the prescribed angle, due to the non-uniformity of the transmitting B_1^+ field [3]. To perform spatial correction of the FA, additional measurement of the B_1^+ field must be included in the scanning protocol. Bloch-Siegert-mapping is a method that performs well in terms of scan time [4]. A description of the method is given in section 2.2.3.

VFA methods using a linearized fit have been shown to overestimate T_1 values [3, 5]. Stikov et al. [3] found that even nonlinear fitting methods lead to a bias towards higher T_1 values when compared to gold standard IR T_1 mapping. This thesis aims at overcoming this error by using a properly regularized MBR approach.

1.1.4 Model-based Reconstruction

Model-based Reconstruction incorporates the signal equation of the used MRI sequence into a minimization problem [6, 7, 8]. The signal equation $S(u)$, holding the analytical relationship between the MR signal and the unknown tissue parameters e.g. $u = (M_0, T_1)$, is used to create a forward model $\mathcal{A}(u)$, which maps the unknown parameters to the space of the present data d. The process of parameter quantification can then be described as varying the parameters in the forward model and comparing the model generated data with the measured data. The ideal parameter estimate as a result is the one that minimizes the difference between the two.

The basic minimization problem (1.4) consists of a L^2-data fidelity term and a regularization term $\mathcal{R}(u)$. The data fidelity term minimizes the described difference between model and data by means of a L_2-norm, while the regularization term, allows for including additional information, based on a priori knowledge of the data. The use of regularization allows for higher degrees of undersampling, which reduces the generally long acquisition time [9].

$$u^{\star} = \arg\min_{u} \|\mathcal{A}(u) - d\|_2^2 + \lambda \mathcal{R}(u) \tag{1.4}$$

In this work parameter quantification is performed using the MBR approach in combination with a FLASH signal model. Detailed explanations on the building of the cost function, the choice of regularization and the solution of the optimization problem are given in chapter 2.

1.1.5 Flip Angle Selection

It is agreed that the right choice of FA is crucial for the performance of the VFA method and the accuracy of the estimated T_1-map [2, 3, 10, 11, 12, 13]. Much research was devoted to finding the right FA for optimal T_1 accuracy and efficiency. A multitude of FA sets was suggested with ranges from two to ten FAs. Although it could be agreed on ideal angles for the dual angle case, much controversy exists as to how many FAs should be used.

The flip angle which yields the maximum signal intensity, is called Ernst angle and can be calculated from $\cos^{-1}(E_1)$. Deoni et al. [2] found that the ideal FAs for a certain T_1 are the ones with a signal intensity corresponding to 71% of the maximum signal. They further derived an analytic expression to calculate these flip angels:

$$\alpha = \cos^{-1}\left(\frac{f^2 E_1 \pm \left(1 - E_1^2\right)\sqrt{1 - f^2}}{1 - E_1^2\left(1 - f^2\right)}\right), \tag{1.5}$$

where $f = 0.71$. Figure 1.2 shows the Ernst angle and the ideal angles for some T_1 values.

Multiple research groups using different selection approaches arrived at the same dual angle set [10]. The dual angle set obtained from equation 1.5 is ideal for the T_R to T_1 ratio it is tuned to. High efficiency can be observed for a certain T_1 range, according to

[11] the range is roughly ±20% of the original T_1. Therefore dual angle sets should be used for small expected T_1 ranges and additional angles should be included for the evaluation of wider T_1 ranges.

The ideal ten angle set is somewhat harder to obtain and different approaches have been suggested. A frequently used ten angle set for brain T_1 mapping was computed by Deoni et. al [12] using a *genetic algorithm*.

In terms of precision it was found that the 10 angle set does not outperform the ideal angles until T_1 becomes larger than 2000 ms, see figure 1.3. Clinically relevant T_1 values range from 20 to 2000 ms. Scan time should be invested in averaging the dual angle data rather than in the acquisition of additional angles. T_1 times found in brain tissue, see table 2.4, do not exceed 2000ms. Cerebrospinal Fluid (CSF) being the exception, with values over 4000ms.

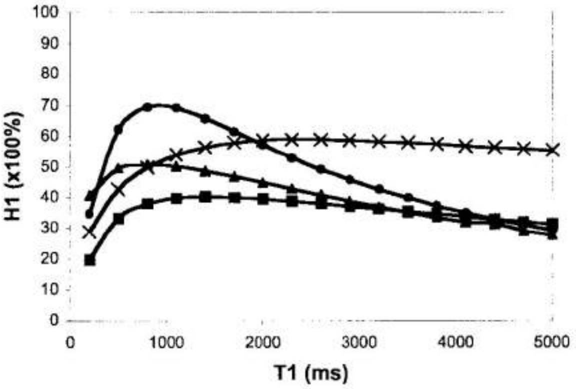

Figure 1.3: Comparison of a set of two ideal angles (circle) with 10 angle sets, in terms of precision over a range of longitudinal relaxation times T_1. For T_1 <2000 ms the two angle set performs best. For higher T_1 values a ten angle set from a *genetic algorithm* (cross) [12] performed best. Figure taken from [12].

Cheng et al. [11] finally claimed that using a three angle set, consisting of a combination of two ideal angle sets, one tuned to a low T_1 and the other tuned to a high T_1 of the expected range of T_1 values, outperformed a set of two ideal FAs in terms of accuracy while avoiding the noise-related bias introduced by even larger angle sets. Therefore being the ideal choice of FAs. In contrast to this findings, Lewis et al. [10], searching for a FA selection method that generates the optimal choice for an arbitrary number of FAs, found, that for FA sets greater than two the optimal choice was a repetition of two angles.

In conclusion it can be said that using the linearized DESPOT [2] method the appropriate choice of FA strongly depends on the imaging problem at hand. However, it is yet unclear if the findings obtained hold for model-based T_1 quantification methods.

Hilbert et al. [13] recently proposed that in terms of MBR a larger range of flip angles results in a more robust T_1 estimation. Therefore undersampled FLASH-data should be acquired and the gained scan time should be invested in measuring more flip angles. Parts of the present work will focus on the selection of flip angles and where to optimally invest scan time.

1.1.6 Accelerated T_1 Mapping

The current gold standard for T_1 mapping is an IR spin echo sequence used with multiple Inversion Times (T_Is). Repetition Times (T_Rs) larger than the longest T_1 occurring in the investigated region are required to achieve sufficient recovery of magnetization between successive inversion pulses. This leads to long T_As. Although methods significantly lowering the scan time exist, they usually suffer from sequence-related errors and resultant T_1 times often deviate from the supposedly true values obtained with IR, especially for in vivo measurements. While Look-Locker methods consistently underestimate the IR T_1 values, the VFA approach consistently overestimates them [3]. Two promising methods in terms of scan time reduction and accuracy of fit are Magnetic Resonance Fingerprinting (MRF) [14] and Model-based Reconstruction (MBR).

The concept of MBR was already outlined in section 1.1.4. A description of an algorithm for model-based T_1 quantification on image data as well as on k-space data is given in section 2.1.1.2 and section 2.2.1 respectively. Their acceleration potential is subject of this work and will be investigated in the course of it.

MRF uses an approach that differs fundamentally from most classical T_1 mapping methods. While those methods are mostly based on a series of images obtained under variation of a single scanning parameter, MRF relies on varying multiple acquisition parameters (FA, T_R and measurement trajectory) in a pseudorandom fashion. While rendering the resulting images useless for evaluation, the process generates a unique signal evolution, referred to as fingerprint, for each tissue. A database containing simulations of all physiologically possible signal evolutions that may be measured serves as a dictionary. A pattern recognition algorithm is used to find the entry that agrees best with the measured fingerprint. A matching dictionary entry consequently yields all parameters used to simulate this entry, allowing for a mapping of multiple parameters, e.g. T_1, T_2, PD, B_1^+.

1.2 Definition of Task

MBR methods for quantitative T_1 mapping, working on either image data or k-space data, should be tested in terms of their stability to different scanning scenarios. T_1 estimation is performed under different SNR levels and FA choices. Further, the acceleration potential of the model-based T_1 quantification should be determined in vivo for highly subsampled data. The MBR algorithms used in this work should be based upon the VFA model. Special thought should be given to minimizing the methods sensitivity to the choice of FAs and its sensitivity to B_1^+ field inhomogeneities. To this end, numerical simulations and statistical evaluations of the proposed algorithms are performed prior to in vivo studies.

2 Methods

In order to find the optimal scanning parameters for the proposed MBR method, numerical simulations are carried out prior to the in vivo brain measurements.

Three different phantoms are used. Two represent simple $N \times M$ grids with a fixed number of pixels for each modelled tissue region, to allow for statistical evaluation. A small 2×2 grid is used for simulations with typical T_1 values in the brain, with each field modelling one tissue (brain grid phantom). A larger 2×7 grid was used to illustrate behaviour over a larger range of T_1 values (NIST [15] grid phantom). For a ROI based evaluation an anatomical human brain phantom generated with MRiLab [16] was used.

T_1 and M_0 values based on previously reported brain measurements at 3 Tesla were assigned to the fields of the small grid phantom and the discrete anatomy of the brain phantom. The tissues modelled were White Matter (WM), Gray Matter (GM) and CSF, with their respective T_1 times, 900, 1400 and 4500 ms. A T_1 of 1150 ms, the mean value of WM and GM, was included in the brain grid phantom. Starting from the T_1 and M_0 maps, representing the ground truth, image data was generated using the FLASH equation 1.1. Phantoms where further tuned to fit the imaging problem at hand by incooperating expected SNR levels and B_1^+ inhomogeneities. The noise at a certain SNR level was calculated using the mean signal at the Ernst angle. The noisy image im_{noise} was obtained from the clean image im by $im_{noise} = \sqrt{(im + \sigma_{gauss})^2 + (\sigma_{gauss})^2}$ accounting for the rician distribution of noise in the magnitude image. The resulting SNR ratio provided the basis for adaption to other resolutions or subsampling scenarios used.

For the large grid phantom T_1 values were taken from the ISMRM/NIST MRI System Phantom [15] and ranged from 22 ms to 2048 ms. M_0 values were varied from 0.8 to 1, and randomly paired with the T_1 values.

T_R was 5 ms for all simulations. With the FAs α being the only unknown, the grid phantoms were used to determine the ideal dual FA sets with a brute force algorithm based on DESPOT described in section 2.1.2. All FA sets to be used in the in vivo measurements were then tested by obtaining T_1 maps using the linearized DESPOT fit 1.1.3, and a model-based method described in section 2.1.1.

2.1 Image-space Based T_1 Quantification

T_1 quantification in the image space operates on a series of FLASH images acquired under different flip angles. Two approaches were used in the present work, both of them making use of the corresponding FLASH signal equation.

The conventional DESPOT method linearizes the signal equation and performs pixel wise linear regression over the flip angles.

MBR follows the scheme outlined in section 1.1.4 with the FLASH signal equation 1.1 representing the model $S(u)$. The problem of finding the parameters M_0 and T_1 is solved by minimizing the difference between the model generated image S(u) and the reconstructed image I.

$$u^\star = \arg\min_u \|S(u) - I\|_2^2 \tag{2.1}$$

Due to the non-linearity of the model $S(u)$ an IRGN-framework is used for the solution of the problem [17].

Three different regularization strategies $\mathcal{R}(u)$ are implemented and described in section 2.1.1.2

2.1.1 Algorithms

2.1.1.1 DESPOT

As described briefly in 1.1.3 the fitting algorithm subsequently yields slope and intercept of the regression line, which hold the M_0 and T_1 estimates and allow for their calculation. Rewriting the linearized problem 1.2 in vector-matrix notation $Ax = d$ by stacking slope m and intercept b for each pixel in the vector x (2.2) and defining the system matrix A (2.3) yields:

$$x = \begin{pmatrix} m_1 \\ \vdots \\ m_N \\ b_1 \\ \vdots \\ b_N \end{pmatrix} \in \mathcal{R}_+^{2N_xN_y \times 1} \tag{2.2}$$

$$A = \begin{pmatrix} \frac{S_{FLASH}}{\tan\alpha_{1,1}} & 0 & 0 & \cdots & 0 & 1 & 0 & \cdots & 0 \\ \frac{S_{FLASH}}{\tan\alpha_{2,1}} & 0 & 0 & \cdots & 0 & 1 & 0 & \cdots & 0 \\ \vdots & \vdots & \vdots & \ddots & \vdots & \vdots & \vdots & \ddots & \vdots \\ \frac{S_{FLASH}}{\tan\alpha_{N_\alpha,1}} & 0 & 0 & \cdots & 0 & 1 & 0 & \cdots & 0 \\ 0 & \frac{S_{FLASH}}{\tan\alpha_{1,2}} & 0 & \cdots & 0 & 0 & 1 & \cdots & 0 \\ 0 & \frac{S_{FLASH}}{\tan\alpha_{2,2}} & 0 & \cdots & 0 & 0 & 1 & \cdots & 0 \\ \vdots & \vdots & \vdots & \ddots & \vdots & \vdots & \vdots & \ddots & \vdots \\ 0 & 0 & 0 & \cdots & \frac{S_{FLASH}}{\tan\alpha_{N_\alpha,N}} & 0 & 0 & \cdots & 1 \end{pmatrix} \in \mathcal{R}_+^{N_xN_yN_\alpha\times 2N_xN_y} \tag{2.3}$$

$$d = \begin{pmatrix} \frac{S_{FLASH}}{\sin\alpha_{1,1}} \\ \vdots \\ \frac{S_{FLASH}}{\sin\alpha_{N_\alpha,1}} \\ \vdots \\ \frac{S_{FLASH}}{\sin\alpha_{N_\alpha,N}} \end{pmatrix} \in \mathcal{R}_+^{2N_xN_y\times 1} \tag{2.4}$$

For the conventional DESPOT method the pixelwise solution of the problem is given by simple matrix inversion $x = A^{-1}d$.

A TV regularized DESPOT approach is introduced with the MBR algorithm in k-space (section 2.2.1), where it serves the method as an initial parameter guess and is used for parameter scaling.

2.1.1.2 Model-based Reconstruction in Image-space

IRGN-Total Generalized Variation (TGV) for (M_0, T_1) Parameter-Mapping using undersampled FLASH-measurements and multiple flip-angles.

Starting from the FLASH-signal equation, neglecting T_2^* relaxation:

$$S\left(M_0, T_1, \alpha_k\right) = M_0 \sin \alpha_k \frac{1 - e^{-\frac{T_R}{T_1}}}{1 - e^{-\frac{T_R}{T_1}} \cos \alpha_k} \tag{2.5}$$

Where:

M_0 : Unknown M_0-map $\in \mathbb{R}_+^{N_x \times N_y}$ with $N_x, N_y \in \mathbb{N}_+$
T_1 : Unknown T_1-map $\in \mathbb{R}_+^{N_x \times N_y}$ with $N_x, N_y \in \mathbb{N}_+$
α_k : Known flip angle $\in \mathbb{R}_+^{N_x \times N_y \times N_\alpha}$ with $N_x, N_y, N_\alpha \in \mathbb{N}_+$
k : Number of flip angles with $k = 1, \ldots, N_\alpha$

the problem of finding M_0 and T_1 can be written as minimization problem:

$$u^\star = \arg\min_u \frac{1}{2} \left\| S(u) - I \right\|_2^2 \tag{2.6}$$

Where:

u : vector of M_0, $T_1 \in \mathbb{R}_+^{2 \times N_x N_y}$
I : reconstructed image $\in \mathbb{C}^{N_x \times N_y \times N_\alpha}$
$S : X \to Y$

The operator S is defined as follows:

$$S : u \to \begin{pmatrix} S\left(M_0, T_1, \alpha_k\right) \\ \vdots \end{pmatrix} \tag{2.7}$$

This problem is non-linear and we employ a Gauss-Newton (GN) approach to find the optimal solution. The GN algorithm consists of a Tayler-series expansion truncated after the first-order term of the non-linear model:

$$S(u) \approx S(u_k) + \underbrace{\frac{\partial S}{\partial u}|_{u=u_k}}_{\text{DS}} \underbrace{(u-u_k)}_{\Delta u} \tag{2.8}$$

The first order Taylorseries term is called DS and can be calculated as follows:

$$\begin{aligned} DS : \Delta u = \begin{pmatrix} \Delta M_0 \\ \Delta T_1 \end{pmatrix} \rightarrow \Bigg(& \frac{\partial S}{\partial M_0}\bigg|_{M_0=M_{0k}, T_1=T_{1k}} \Delta M_0 + \\ & \frac{\partial S}{\partial T_1}\bigg|_{M_0=M_{0k}, T_1=T_{1k}} \Delta T_1 \Bigg) = y \end{aligned} \tag{2.9}$$

The derivatives of the signal model S(u) with respect to M_0 and T_1 are:

$$\frac{\partial S}{\partial M_0} = \sin\alpha \, \frac{1-e^{-\frac{T_R}{T_1}}}{1-e^{-\frac{T_R}{T_1}}\cos\alpha} \tag{2.10}$$

$$\frac{\partial S}{\partial T_1} = -\frac{M_0 T_R e^{\frac{T_R}{T_1}} \left(2\sin\alpha - 2\cos\alpha\sin\alpha\right)}{2{T_1}^2 \left(e^{\frac{T_R}{T_1}} - \cos\alpha\right)^2} \tag{2.11}$$

Yielding the so called inner problem of the GN approach:

$$\begin{aligned} & \|S(u) - I\|_2^2 \rightarrow \\ & \|S(u_k) + DSu - DSu_k - I\|_2^2 \rightarrow \\ & \|DSu + \underbrace{S(u_k) - DSu_k - I}_{\tilde{I}}\| \end{aligned} \tag{2.12}$$

This linearized data term is further extended by a step size penalty and a regularization term $R(u)$. The step size penalty is defined as the squared L_2-norm of the difference between linearization point u_k and current parameter estimate u. This limits the allowed descent along the linearized function in each Gauss-Newton (GN) step and results in a strongly convex subproblem with convexity parameter δ.

$$u_{k+1}^{\star} = \arg\min_{u} \frac{\lambda}{2} \sum_{i=1}^{N_\alpha} \|DS_{\alpha_i} u - \tilde{I}_{\alpha_i}\|_2^2 + \frac{\delta}{2}\|u - u_k\|_2^2 + \mathcal{R}(u) \tag{2.13}$$

Three different regularization methods were implemented. Simple L^2 regularization uses only the step size penalty, reducing the the regularization term $R(u)$ in equation 2.13 to zero.

A functional that has proven to perform well as a regularization term for natural and medical image reconstruction is the 2^{nd}-order Total Generalized Variation (TGV^2) [18]. TGV^2 regularization constitutes itself a minimization problem and is of the form:

$$TGV_\alpha^2(u) = \min_{w} \; \alpha_1 \|\nabla u - w\|_1 + \alpha_0 \|\mathcal{E}w\|_1 \tag{2.14}$$

with the operator ∇ corresponding to finite forward differences, $\mathcal{E}$ being the symmetrized derivative $\mathcal{E}w = \frac{1}{2}(\nabla w + \nabla w^T)$, and a set of adjustable positive weights α_0 and α_1 used to balance between the first and second derivative. The use of higher order derivatives of the function u in TGV^2, reduces the staircasing effect, often observed over image regions of smooth or linear varying contrast, when using e.g. Total Variation (TV) regularization [19].

In this work TGV^2 regularization is implemented in two forms. TGV_{sep}^2 (see 2.15a) includes a TGV^2 regularization functional for each parameter e.g. M_0 and T_1, while in TGV_{frob}^2 [20] (see 2.15b), the functionals are joined by using a Frobenius norm on the parameter maps. The multiparametric functional of TGV_{frob}^2 exploits shared features across parameter maps [17].

$$TGV_{sep}^2(u) = TGV_{\alpha}^2(M_0) + TGV_{\alpha}^2(T_1) \tag{2.15a}$$

$$TGV_{frob}^2(u) = \min_{w} \; \alpha_1 \| |\nabla u - w|_{frob} \|_1 + \alpha_0 \| |\mathcal{E} w|_{frob} \|_1 \tag{2.15b}$$

L^2 regularisation results in the following minimization problem that can be solved with the Conjugate Gradient (CG) algorithm described in algorithm 2.

$$\begin{aligned} u^{\star} &= \arg\min_{u} \; \frac{\lambda}{2} \| DSu - \tilde{I} \| + \frac{\delta}{2} \| u - u_k \|_2^2 \\ &\rightarrow \lambda DS^H \left(DSu^{\star} - \tilde{I} \right) + \delta (u^{\star} - u_k) = 0 \\ &\rightarrow \lambda DS^H DSu^{\star} - \lambda DS^H \tilde{I} + \delta u^{\star} - \delta u_k = 0 \\ &\rightarrow \underbrace{\left(\lambda DS^H DS + \delta \right)}_{M} u^{\star} = \underbrace{\lambda DS^H \tilde{I} + \delta u_k}_{rhs} \\ &\rightarrow u^{\star} = M^{-1} rhs \end{aligned} \tag{2.16}$$

The adjoint of DS, termed DS^H is defined as the complex matrix transpose operation:

$$DS^H : y \rightarrow \begin{pmatrix} \sum_{k=1}^{\#\alpha} \overline{\frac{\partial S(\alpha_k)}{\partial M_0}} \Big|_{M_0 = M_{0k}, T_1 = T_{1k}} \\ \\ \sum_{k=1}^{\#\alpha} \overline{\frac{\partial S(\alpha_k)}{\partial T_1}} \Big|_{M_0 = M_{0k}, T_1 = T_{1k}} \end{pmatrix} \tag{2.17}$$

TGV regularization is based on the L_1-norm and therefore adds non-differentiability to the problem. To solve the non-differentiable subproblems of the IRGN method a recently proposed primal-dual algorithm [21] is applied.

The primal dual algorithm can be applied to problems of the form

$$\min_{u} F(Ku) + G(u) \tag{2.18}$$

which is termed the primal problem.

F and G are convex, lower semi-continuous functions, and K is a linear operator. By comparing this primal form to the regularized IRGN subproblem from equation 2.13, F(u) and G(u) can be identified as follows.

$$F(u) = \mathcal{R}(u) \tag{2.19a}$$

$$G(u) = \frac{\lambda}{2}\|DSu - \tilde{I}\| + \frac{\delta}{2}\|u - u_k\|_2^2 \tag{2.19b}$$

The function F(u) and K depend on the chosen regularisation strategy 2.15 a-b and are defined in 2.20 a-b and 2.21 a-b respectively.

$$F(u) = \alpha_1\|p_0\|_1 + \alpha_0\|q_0\|_1 + \beta_1\|p_1\|_1 + \beta_0\|q_1\|_1 \tag{2.20a}$$

$$F(u) = \alpha_1\|p\|_1 + \alpha_0\|q\|_1 \tag{2.20b}$$

$$Kx = \begin{pmatrix} \nabla & 0 & -Id & 0 \\ 0 & 0 & \mathcal{E} & 0 \\ 0 & \nabla & 0 & -Id \\ 0 & 0 & 0 & \mathcal{E} \end{pmatrix} \underbrace{\begin{pmatrix} M_0 \\ T_1 \\ v_0 \\ v_1 \end{pmatrix}}_{x} \tag{2.21a}$$

$$Kx = \begin{pmatrix} \nabla & -Id \\ 0 & \mathcal{E} \end{pmatrix} \underbrace{\begin{pmatrix} u \\ v \end{pmatrix}}_{x} \tag{2.21b}$$

K^H, see equations 2.22, holds the adjoint operations of K, with the divergence operator div^1 being the negative adjoint of the operator ∇ and div^2 the one of symmetrized derivative $\mathcal{E}$.

$$K^H y = \begin{pmatrix} -div_1 & 0 & 0 & 0 \\ 0 & 0 & -div_1 & 0 \\ Id & -div_2 & 0 & 0 \\ 0 & 0 & Id & -div_2 \end{pmatrix} \underbrace{\begin{pmatrix} p_0 \\ q_0 \\ p_1 \\ q_1 \end{pmatrix}}_{y} \tag{2.22a}$$

$$K^H y = \begin{pmatrix} -div_1 & 0 \\ -Id & -div_2 \end{pmatrix} \underbrace{\begin{pmatrix} p \\ q \end{pmatrix}}_{y} \tag{2.22b}$$

In order to use the primal-dual formalism one needs the proximal mapping operator of $F^*(u)$, which represents the convex conjugate of $F(u)$. The convex conjugate $f^*(y)$ is defined by

$$\begin{aligned} f^*(y) &= \sup_x \langle x, y\rangle - f(x) \\ f(Kx) &= \sup_x \langle Kx, y\rangle - f^*(y) \end{aligned} \tag{2.23}$$

and transforms a function $f(x)$, independent of its convexity into a convex function.

The general update steps of the primal-dual algorithm are defined as:

$$\begin{aligned} y^+ &= (I + \sigma\partial F^*)^{-1}(y + \sigma K\overline{x}) \\ x^+ &= (I + \tau\partial G)^{-1}(x - \tau K^H y^+) \\ \overline{x}^+ &= 2x^+ - x \end{aligned} \tag{2.24}$$

with $\tau, \sigma > 0$ denoting the primal and dual step size. In order to ensure convergence of the algorithm the step size is chosen such that $\sigma\tau L^2 < 1$ [22]. The operator norm is defined as $L = \|K\|_2$ and calculated to be $\sqrt{12}$, thus giving $\tau = \sigma = \frac{1}{\sqrt{12}}$.

Proximal mapping, dual update:

For TGV^2_{sep} (2.15a) and TGV^2_{frob} (2.15b), The convex conjugate $F^*(u)$ consists of a repetition of indicator functions.

$$F^*(u) = I_{\|\cdot\|_\infty \le \alpha_1}(p_1) + I_{\|\cdot\|_\infty \le \alpha_0}(q_1) + I_{\|\cdot\|_\infty \le \beta_1}(p_2) + I_{\|\cdot\|_\infty \le \beta_0}(q_2) \tag{2.25a}$$

$$F^*(u) = I_{\|\cdot\|_\infty \le \alpha_1}(p) + I_{\|\cdot\|_\infty \le \alpha_0}(q) \tag{2.25b}$$

Since the functions are independent with respect to their variables, the proximal mapping can be applied independently on the single functions. The proximal mapping of the indicator function of the infinity norm reduces to pointwise Euclidean projection onto the L_∞ norm ball.

$$\begin{aligned} y_i^+ = prox_{\sigma_f^\star}(\xi) &= (Id + \sigma\partial F^*)^{-1}(\xi) \\ &= \arg\min_y \frac{1}{2\sigma}\|y-\xi\|_2^2 + F^*(u) \\ &= \arg\min_y \frac{1}{2\sigma}\|y-\xi\|_2^2 + I_{\|\cdot\|_\infty \leq \eta} \\ &= \arg\min_{\|y\|_\infty \leq \eta} \frac{1}{2\sigma}\|y-\xi\|_2^2 \\ &\rightarrow \frac{1}{\sigma}(y-\xi) = 0 \\ &\rightarrow y_i = \frac{\xi_i}{\max\left(1, \frac{|\xi_i|}{\eta}\right)} \end{aligned} \tag{2.26}$$

Proximal mapping, primal update:

$$\begin{aligned} u_i^+ = prox_{\tau_g}(\xi) &= (Id + \tau\partial G)^{-1}(\xi) \\ &= \arg\min_u \frac{1}{2\tau}\|u-\xi\|_2^2 + \frac{\lambda}{2}\|DSu - \tilde{I}\| + \frac{\delta}{2}\|u - uk\| \\ &\rightarrow \frac{1}{\tau}(u^\star - \xi) + \lambda DS^H(DSu^\star - \tilde{I}) + \delta(u^\star - u_k) = 0 \\ &\rightarrow \underbrace{\frac{1}{\tau}Id + \delta Id + \lambda DS^H DS}_{M}\, u^\star = \frac{\xi}{\tau} \underbrace{+\lambda\tilde{I} + \delta u_k}_{r_{part}} \\ &\rightarrow u^\star = M^{-1}\left(r_{part} + \frac{\xi}{\tau}\right) \end{aligned} \tag{2.27}$$

2.1.2 Flip Angle Determination

Flip angles are determined with a simple brute force algorithm based on DESPOT T_1 mapping. Using the 2x2 grid tuned to target T_1 values and expected SNR, T_1 maps are evaluated for all possible dual FA combinations from, either a user defined set of FAs, or the expected range of angles, which is determined by the highest T_R to T_1 ratio present in the phantom, see table 2.1. The number of possible combinations of k elements out of a range of n is described by the binomial coefficient $\binom{n}{k}$ and gives the number of iterations needed. The decision criterion for maximum accuracy is given by minimal standard deviation in the resultant T_1-maps. The algorithm returns an ideal FA set for each region, and chooses the set which gives the best overall result for all four regions.

Table 2.1: Depending on the highest T_R to T_1 ratio present in the phantom the bruteforce algorithm searches the ideal dual FA set within a certain FA range.

$\frac{T_R}{T_1}_{max}$ (a.u.)	FA range
> 0.03	$\{1, 2, \ldots, 90\}$
> 0.004	$\{1, 2, \ldots, 30\}$
> 0.002	$\{1, 2, \ldots, 15\}$
≤ 0.002	$\{1, 2, \ldots, 10\}$

After determination and testing of the FAs with the DESPOT method, FA sets to be used for the numeric simulation, as well as for the in vivo brain measurements were chosen as follows. Optimization for brain tissue by a *genetic algorithm* [12] formed the ten angle set $\{2°, 3°, 4°, 5°, 7°, 9°, 11°, 14°, 17°, 22°\}$. For the smaller angle sets, ideal angles are tuned to the mean T_1 of white and grey matter $\frac{T_{1,gm}+T_{1,wm}}{2} = \frac{900+1400}{2} = 1150$ ms, and chosen to be subsets of the ten angle set. Forming a dual angle set $\{2°, 14°\}$ and a triple angle set $\{2°, 14°, 17°\}$. In the ten angle case, the set is tuned to a higher mean T_1 of 2550 ms, which is justified by the better expected performance over the complete range of T_1 values in the brain. Ideal flip angles only hold for a certain T_R to T_1 ratio, see equation 1.5. All flip angle sets used in this work where generated for a T_R of 5ms. In vivo measurements were recorded accordingly.

2.1.3 Flip Angle Verification

The capability of the brute force algorithm to determine ideal angle sets was shown by comparison with angle sets found in the literature, as well as by evaluating T_1 maps generated under usage of the chosen FA sets.

2.1.4 Statistical Evaluation

The chosen flip angle sets and their performance within the different T_1 quantification methods were tested under different scenarios using the 2x2 grid phantom. Their robustness to the SNR of the data was tested for SNR levels of 30, 15 and 5 dB. The influence of an erroneous B_1^+ map on the reconstruction was tested as described in 2.2.3.

2.2 Accelerated Variable Flip Angle T_1 Quantification

A major drawback of performing quantitative MRI with methods operating on image data is their limited acceleration potential. Although techniques like Parallel Imaging (PI) do allow for some acceleration of the measurement process, only moderate AFs are achieved. Further acceleration requires either the use of methods operating on k-space data, or the combination of MBR in image space with a powerful image reconstruction method that allows for high subsampling factors. This thesis presents a comparison of both approaches regarding their acceleration potential, their respective implementations are described in section 2.2.1 and section 2.2.2.

2.2.1 Model-based Reconstruction in k-Space

The IRGN approach for the solution of TGV_{frob}^2 regularized MBR problems was already described in section 2.1.1.2, for the case of image space data. It basically consist in iteratively linearizing the model in each GN step, creating convex inner problems which can be solved with the primal dual algorithm.

Expanding the forward model $\mathcal{A}(u)$ allows for determination of T_1 maps directly from multi-channel raw data. In addition to the used imaging sequence, the new forward model for k-space data encompasses the Fourier transform, the sensitivity profiles of the receiver coils, and the used k-space sampling scheme.

To that effect a new operator A that maps from parameter to k-space is defined:

$$A : u \rightarrow \begin{pmatrix} P_k \mathcal{F} \left[C_i S \left(M_0, T_1, \alpha_k \right) \right] \\ \vdots \end{pmatrix} \tag{2.28}$$

Where:

P_k : Undersampling pattern
C_i : Coil sensitivity profile
$k = 1 \dots N_\alpha$: Number of flip angles
$i = 1 \dots N_{coils}$: Number of coils

The corresponding inner problem is:

$$u^{\star}_{k+1} = \arg\min_{u} \frac{\lambda}{2} \sum_{i=1}^{N_\alpha} \| D A_{\alpha_i} u - \tilde{d}_{\alpha_i} \|_2^2 + \frac{1}{2\delta} \| u - uk \|_2^2 + \mathcal{R}(u) \tag{2.29}$$

with $\mathcal{R}(u) = TGV^2_{frob}$, see equation 2.15b. For comparison see equations 2.7 and 2.13 which hold the definition of the operator S and the inner problem in image space.

The update scheme for the primal dual algorithm in k-space is given in algorithm 5. For detailed information on the optimization framework the interested reader is referred to [17].

Knowledge of the coil sensitivity profiles is needed prior to reconstruction and their determination has to be implemented as a pre-processing step. In the present work coil sensitivities were estimated from fully sampled data even in the subsampling case. In case of highly undersampled data additional scans need to be included for the joint estimation of low resolution images and coil sensitivities. Since high estimate accuracy can be achieved from a single acquisition with only a very small area in the central k-space, the additional scan does not substantially increase the total scan time, therefore making it a feasible method for accelerated T_1 mapping.

2.2.2 ICTGV reconstruction and Model-based Reconstruction in Image-space

Infimal Convolution Total Generalized Variation (ICTGV) is a convex spatio-temporal regularization functional, proposed in the context of reconstruction of dynamic image data [23]. Combining two TGV functionals, with different spatio-temporal weighting, by infimal convolution, ICTGV optimally balances between spatial and temporal regularization. Decomposing the image into two components, it enforces either strong spatial or strong temporal regularization, depending on the local requirements. In the MRI field, ICTGV regularization has been successfully used for the reconstruction of highly-subsampled dynamic MR data [24].

Since VFA data is recorded under variation of the FA α, a parameter dimension is added to the data space, analogue to the temporal dimension in dynamic image data. ICTGV regularization exploits the information across the parameter dimension allowing for subsampling of VFA data. Iterative image reconstruction with ICTGV regularization prior to T_1 parameter quantification was proven to achieve high quality parameter maps up to an AF of 16 [25].

2.2.3 Bloch-Siegert B_1^+ Mapping and Coil Calibration

As stated in section 1.1.3, a B_1^+ transmit field, with a certain nominal flip angle, actually produces a range of flip angles over the image volume, due to inevitable inhomogeneities in the RF field.

To account for these flip angle variations, B_1^+ maps need to be calculated and included in the reconstruction of images or parameter maps. Several methods exist to measure the flip angle distribution [26, 27, 28]. Most of them are signal-magnitude based and suffer from a series of problems [4]. Amongst them T_1 dependency, long acquisition times, and inaccuracy, especially at low flip angles. This factors are especially unfavourable for the T_1 quantification problem at hand. First of all as FLASH makes use of small flip angles, and more generally as the objective was testing the acceleration potential.

Bloch-Siegert B_1^+ mapping [4] is a method that has proven to perform well in terms of accuracy, acquisition time and robustness and is used in the present work. Based on the so called Bloch-Siegert effect it makes use of the signals phase, instead of its amplitude. A Bloch-Siegert shift is the spin precision frequency shift caused by applying an off-resonance RF-pulse, of frequency ω_{RF}. This frequency shift causes a phase shift in the image, which encodes the B_1^+ information. Finally undesired off-resonance effects are cancelled out by taking the difference of two phase images acquired at symmetric off-resonance pulses $\pm\omega_{RF}$, as they have the same phase factors in both images. The resulting phase shift Φ_{BS} depends solely on the Bloch-Siegert effect and is proportional to B_1^+, allowing for its calculation, see equation 2.30.

$$\Phi_{BS} = \int_0^T \frac{(\gamma B_1^+(t))^2}{2\omega_{RF}(t)} dt \tag{2.30}$$

B_1^+ profiles were also incorporated in the phantom generation. The B_1^+ maps in the anatomical brain phantom were generated to represent the variation of flip angles found in our in vivo measurement data. Figure 2.1 shows in vivo (a) and phantom (b) B_1^+ maps juxtaposed for comparison.

In the simple 2x2 grid phantom the flip angle variation was extended to cover the whole grid. The influence of an erroneous B_1^+ map on the performance of the proposed algorithms for T_1 mapping was tested by introducing a ±5% error in the B_1^+ map used for T_1 quantification. Figure 2.2 shows the B_1^+ map used in the grid phantom.

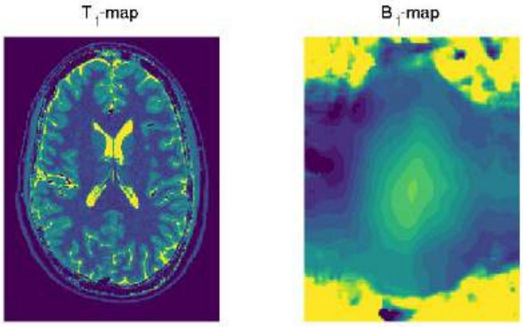

(a) In vivo

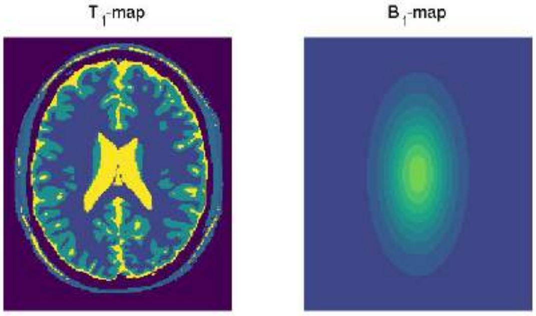

(b) Phantom

Figure 2.1: T_1 and B_1^+ maps for measured in vivo data (a) and as used in the simulations with the anatomical brain phantom (b).

In the case of the image space based T_1 quantification, the coil sensitivity has already been dealt with, in the used image reconstruction method. However, for k-space based methods the coil sensitivity profiles form part of the forward model and therefore of the reconstruction problem. In this work a regularized non-linear inversion method was used for coil sensitivity estimation. This method was proposed [29] and later extended to non-cartesian k-space encoding [30] by Ücker et. all. Validation of the method has been shown for undersampled radial FLASH data in the context of real-time MRI of the human heart [30] as well as for accelerated T_1 mapping [31]. No correction to account for deviations due to imperfections in the gradient systems is performed.

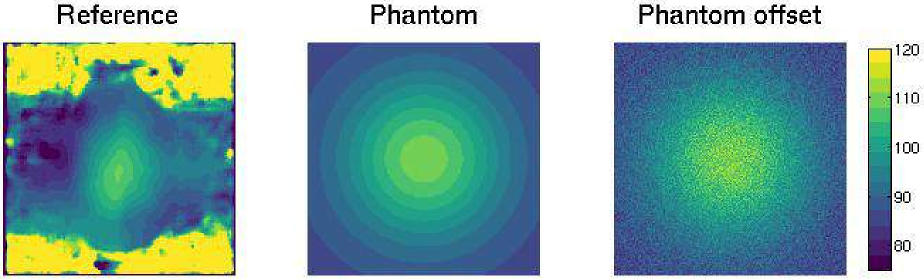

Figure 2.2: From left to right: B_1^+ map used for Reference, B_1^+ map in the phantom, B_1^+ map with an ±5% error.

2.2.4 Data Acquisition

In vivo brain data of three healthy male volunteers was recorded on a clinical 3T MAGNETOM Skyra scanner (Siemens Healthineers, Erlangen, Germany) using a 32-channel head coil. The in-plane resolution was 1 mm^2 in all cases, the slice thickness was varied from 1 to 5 mm across subjects. A FLASH sequence was employed to generate VFA data, as described in section 1.1.3. The used scanning protocol can be found in table 2.2.

High frequency RF-Pulses can lead to a temperature increase in the subject. The deposition of energy in the subjects tissue in relation to its body weight is called Specific Absorption Rate (SAR). To monitor the heating of patient tissue, the MR scanner estimates the SAR based on the scanning parameters and the weight of the subject, before running the measurement protocol. If the SAR limits are exceeded, possible options for lowering the values are increased T_Rs, longer RF-pulses which allow for lower pulse amplitudes, or the usage of smaller flip angles. In the highest resolution case ($1mm^3$ isotropic resolution, volunteer 1) SAR levels were too high for the 22° angle measurement. In terms of keeping the T_R time constant, the 22° FA was omitted and a smaller flip angle at 12° was included in the 10 angle set, for volunteer 1.

T_1 quantification of in vivo data was realized as follows. Only full ten angle sets where used for image space based T_1 quantification, since the upstream image reconstruction

Table 2.2: Scanning parameters and flip angle sets used for the in vivo brain measurements. Slice thickness was varied from 1 to 5 mm across subjects. For all scans $T_R = 5$ ms and $T_E = 2.46$ ms was used.

	Scanning Protocol		
	Volunteer 1	Volunteer 2	Volunteer 3
Resolution (mm^3)	$1 \times 1 \times 1$	$1 \times 1 \times 3$	$1 \times 1 \times 5$
Matrix size	$256 \times 256 \times 36$	$256 \times 256 \times 36$	$256 \times 256 \times 22$
10 angle set (°)	{2, 3, 4, 5, 7, 9, 11, 12, 14, 17}	{2, 3, 4, 5, 7, 9, 11, 14, 17, 22}	{2, 3, 4, 5, 7, 9, 11, 14, 17, 22}
3 angle sets (°)		{2, 14, 17} {2, 14, 14}	
2 angle set (°)		{2, 14}	

algorithm AVIONIC (ICTGV) [24] does not allow for the reduction of flip angles. k-Space based T_1 quantification using the 10 angle set was performed alike. Additionally a comparison of the performance of different flip angle sets was performed for volunteer 2 by taking two and three angle subsets out of the 10 angle set. These sets matched the ones generated with the brute force algorithm and used in the numerical simulations. Two subsets were evaluated in the three angle case, $\{2°, 14°, 14°\}$ and $\{2°, 14°, 17°\}$.

2.2.4.1 Radial Volumetric Encoding Sequence

Measurements were performed using the Radial Volumetric Encoding (RAVE) sequence with a Golden Angle (GA) ordering scheme [32]. This radial sampling scheme shifts consecutive spokes by the Golden Angle Φ_{GA}=111,25°, with each spoke filling the largest gap between the previously sampled ones. This guarantees optimal k-space coverage for any arbitrary number of spokes, especially for numbers drawn from the Fibonacci series, see figure 2.3.

For a number of read-out samples per spoke $N_{readout}$, fulfilling the Nyquist criterion $\Delta k_{readout} = 1/\text{FOV}$, the number of spokes required for artefact free reconstruction corresponds to $N_{spokes} = \frac{\pi}{2} \cdot N_{readout}$. This ensures that the angular sampling distance does

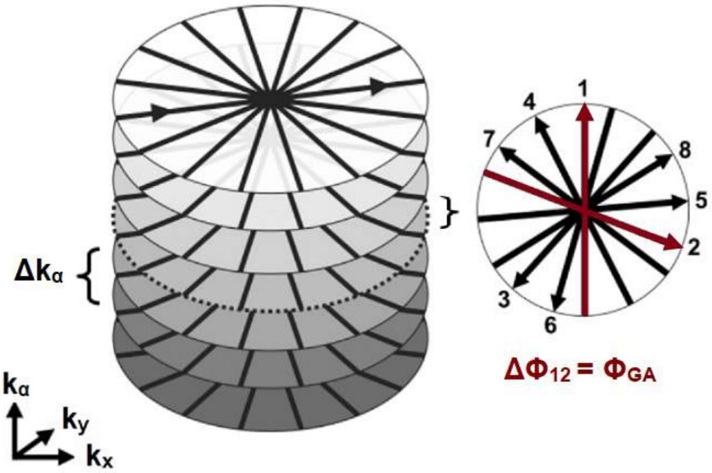

Figure 2.3: Golden angle ordering scheme [32]. Numbers indicate the acquisition order of the radial spokes. The angle between two consecutive spokes Φ_{GA} is 111,25°. Figure adapted from [33].

not exceed the read-out sampling distance $\Delta k_{angular} \leq \Delta k_{readout}$ and holds for uniform spacing. [32]

Fully sampled data was recorded with a matrix size of $256 \times 256 \times 36(22)$, see table 2.2, and 550 spokes, satisfying $N_{spokes} \geq \frac{\pi}{2} \cdot 256 = 402$. The Generation of subsampled data is implemented as a post-processing step, and consists in selecting a Fibonacci number of consecutive spokes for each frame. The scheme is continued across frames (flip angle variation), the first spoke of a new frame being shifted by the GA in respect to the last one of the old frame. The used Spokes per Frame (SPF) and corresponding AFs are summarised in table 2.3. Basis for the calculation of AFs was a fully sampled cartesian acquisition with 256 phase encoding steps N_{phase}. The Acquisition Time in this case is 12.8 seconds per slice, according to $T_A = N_{phase} \cdot T_R \cdot N_\alpha$.

In the subsampling case, averaging of dual or triple angle data corresponds to rising the number of acquired spokes per frame, by multiplying them with the number of averages, in terms of SNR gain. Since the stability of the reconstruction is determined by the SNR level as well as by the amount of subsampling (number of SPF), scan time was invested

Table 2.3: T_1 maps were evaluated for six different Acceleration Factors AF. For the ten angle case the number of Spokes per Frame (SPF) was chosen from the Fibonacci series. The Acquisition Time (T_A) was kept constant over different angle sets by adapting the number of SPF.

AF	4.7	7.5	12.2	19.7	32	51
T_A/slice (s)	2.75	1.70	1.05	0.65	0.4	0.25
SPF (10 FA)	55	34	21	13	8	5
SPF (3 FA)	183	113	70	43	27	17
SPF (2 FA)	225	170	105	65	40	25

in more spokes.

2.2.5 ROI-based Evaluation

For the evaluation of the T_1 quantification from in vivo data, masks separating the tissue present in the evaluated slices, were generated for each subject. In total five Regions of Interest (ROIs), corresponding to Gray Matter (GM), White Matter (WM), Caudate Nucleus (CN), Putamen (P) and Cerebrospinal Fluid (CSF), were defined. Mean and standard deviation of the estimated T_1 values were computed for each ROI and compared to literature values. T_1 maps from fully sampled data were generated using the TGV^2_{frob}-regularized MBR approach on ICTGV reconstructed image data and served as a reference for accelerated T_1 mapping. The same ROIs were used across mapping methods, acceleration factors and flip angle sets. Comparison for different slice thicknesses, respectively SNR levels, was performed for WM and GM only, as these were the tissues present in all selected slices.

Reported T_1 values for the same tissue and field strength vary greatly for different T_1 mapping techniques. For white matter estimated T_1 values range from 690 ms to 1100 ms. Even with the IR method, which is considered to be the gold standard for T_1 mapping, the variation is larger than 50% [3].

Table 2.4 shows reference values obtained with IR spin echo protocols at 3 Tesla [34, 35].

Variation of the voxel volume has a significant impact on the T_1 estimates. Different SNR levels introduce a noise related bias to the estimates and an increase in slice thickness introduces partial volume effects to the images. Especially cortical gray matter suffers from partial volume effects of white matter or cerebrospinal fluid [11]. Therefore the measured slice thickness was taken into account when searching for reference values.

Table 2.4: T_1 reference values found in literature for gold standard T_1 mapping. Mean ± standard deviation T_1 of different brain tissues are listed under consideration of the measured slice thickness.

	2 mm [34]	5 mm [35]
WM	913 ± 23 885 ± 47	791 ± 27
GM		1445 ± 119
P	1275 ± 50	
CN	1424 ± 50	1271 ± 91
CSF		4163 ± 263

3 Results

3.1 Numerical Simulation

3.1.1 Flip Angle Selection

Table 3.1 shows the good agreement of the dual FA sets generated with the brute force algorithm, described in 2.1.2, with those found in literature [36].

Table 3.1: Dual FA sets for a variety of T_R to T_1 ratios. Comparison between sets generated with the brute force algorithm and literature values [36].

T_1**(ms)**	$\frac{T_R}{T_1}$**(a.u.)**	**flip angle (°)**	**reference (°)**
17	0.3	{18, 87}	{18, 86}
25	0.2	{15, 76}	{15, 75}
31	0.16	{13, 71}	{13, 69}
50	0.1	{10, 55}	{11, 57}
63	0.08	{10, 56}	{9, 51}
100	0.05	{7, 45}	{7, 42}
125	0.04	{7, 37}	{7, 38}
250	0.02	{5, 27}	{5, 27}
333	0.015	{4, 24}	-
500	0.01	{3, 20}	-
714	0.007	{3, 17}	-
1000	0.005	{2, 12}	{2, 13}
1500	0.003	{2, 10}	-
2000	0.0025	{2, 9}	-

3.1.2 Robustness to SNR Level

The Performance of the proposed T_1 quantification methods in dependence of the SNR of the data was tested with the brain grid phantom. T_1 values were evaluated for the four ROIs modeled in the phantom, i.e. White Matter (WM), $T_{1,mean}$, Gray Matter (GM) and Cerebrospinal Fluid (CSF), under three different SNR levels. Different numbers of FAs were included in the evaluation. SNR levels were 30, 15 and 5 dB, FA sets used were $\{2°, 14°\}$, $\{2°, 14°, 17°\}$ and $\{2°, 3°, 4°, 5°, 7°, 9°, 11°, 14°, 17°, 22°\}$.

For SNR levels of 30, 15 and 5, figures 3.1 to 3.3 show the median and the 25% and 75% percentile, i.e. the first and third quartile, of the T_1 estimates, visualising the results. The hypothetical scanning time in each case was held constant by averaging the data of the smaller angle sets. To that effect, three angle sets were averaged three, and two angle sets five times. Stated SNR levels apply to the ten angle set, the other sets show an improved SNR = SNR $\times\sqrt{N_{av}}$, with N_{av} being the number of averages. Corresponding to figure 3.1 to 3.3, tables 3.2 to 3.4 show mean and standard deviation of the estimated T_1 values for the DESPOT method and the TGV^2_{frob}-regularized MBR approach.

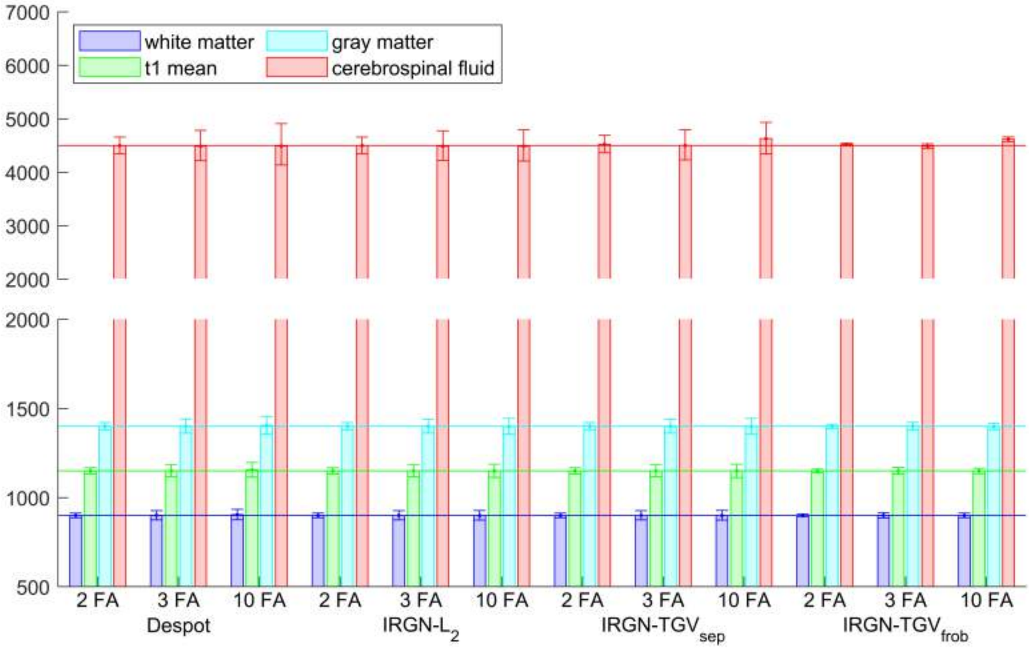

Figure 3.1: Performance of the proposed T_1 mapping methods at a SNR of 30 dB. Median, first and third quartile of T_1 estimates for the four ROIs of the brain grid phantom. T_A constant for different FA sets.

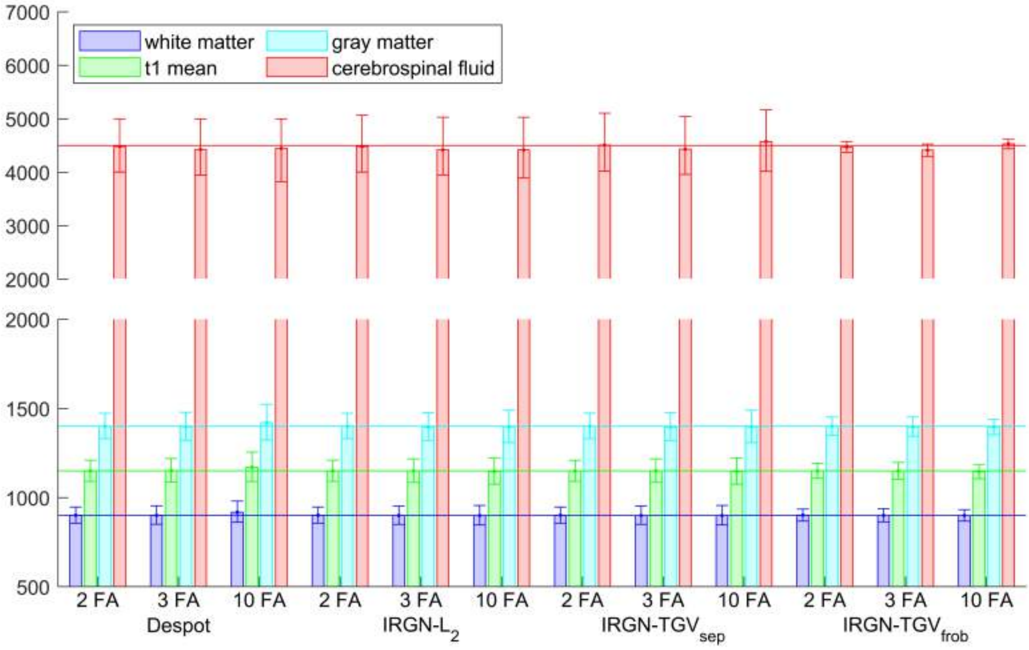

Figure 3.2: Performance of the proposed T_1 mapping methods at a SNR of 15 dB. Median, first and third quartile of T_1 estimates for the four ROIs of the brain grid phantom. T_A constant for different FA sets.

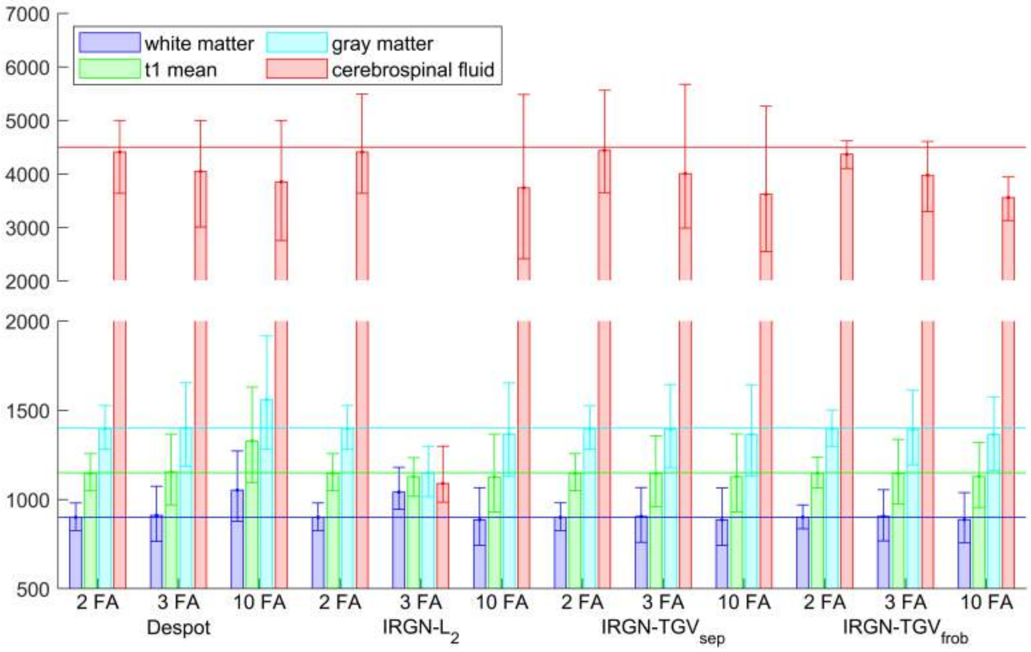

Figure 3.3: Performance of the proposed T_1 mapping methods at a SNR of 5 dB. Median, first and third quartile of T_1 estimates for the four ROIs of the brain grid phantom. T_A constant for different FA sets.

Table 3.2: Performance of the DESPOT method and the TGV^2_{frob}-regularized MBR approach at a SNR of 30 dB. Mean ± standard deviation of T_1 estimates for the four ROIs of the brain grid phantom. T_A constant for different FA sets.

	WM	$T_{1,mean}$	GM	CSF
Reference	900	1150	1400	4500
Despot				
2 FA	900 ± 19	1150 ± 25	1400 ± 31	4505 ± 226
3 FA	901 ± 38	1151 ± 50	1402 ± 59	4483 ± 356
10 FA	905 ± 44	1157 ± 61	1407 ± 74	4465 ± 441
$\boldsymbol{TGV_{frob}}$				
2 FA	900 ± 12	1150 ± 15	1400 ± 17	4510 ± 69
3 FA	901 ± 23	1151 ± 29	1401 ± 33	4482 ± 84
10 FA	900 ± 20	1149 ± 24	1399 ± 27	4603 ± 110

Table 3.3: Performance of the DESPOT method and the TGV^2_{frob}-regularized MBR approach at a SNR of 15 dB. Mean ± standard deviation of T_1 estimates for the four ROIs of the brain grid phantom. T_A constant for different FA sets.

	WM	$T_{1,mean}$	GM	CSF
Reference	900	1150	1400	4500
Despot				
2 FA	903 ± 67	1153 ± 89	1405 ± 105	4411 ± 540
3 FA	903 ± 77	1154 ± 100	1403 ± 118	4375 ± 560
10 FA	923 ± 90	1177 ± 123	1429 ± 151	4325 ± 662
$\boldsymbol{TGV_{frob}}$				
2 FA	902 ± 52	1151 ± 66	1402 ± 77	4466 ± 165
3 FA	901 ± 57	1151 ± 72	1399 ± 84	4407 ± 195
10 FA	900 ± 52	1147 ± 63	1396 ± 69	4512 ± 166

Table 3.4: Performance of the DESPOT method and the TGV^2_{frob}-regularized MBR approach at a SNR of 5 dB. Mean ± standard deviation of T_1 estimates for the four ROIs of the brain grid phantom. T_A constant for different FA sets.

	WM	$T_{1,mean}$	GM	CSF
Reference	900	1150	1400	4500
Despot				
2 FA	907 ± 117	1158 ± 156	1411 ± 186	4249 ± 756
3 FA	931 ± 239	1187 ± 315	1446 ± 373	3898 ± 1069
10 FA	1105 ± 332	1409 ± 466	1667 ± 565	3746 ± 1154
$\boldsymbol{TGV_{frob}}$				
2 FA	905 ± 103	1155 ± 135	1405 ± 157	4339 ± 428
3 FA	920 ± 224	1169 ± 285	1422 ± 330	3947 ± 985
10 FA	910 ± 223	1153 ± 285	1388 ± 328	3489 ± 695

To further allow for comparison of FA sets within a certain SNR level, SNR was kept constant in the 15 dB case i.e. no averaging of the small FA sets was performed. This effectively reduces the scan times for the smaller angle sets. Figure 3.4 again shows the median as well as the first and third quartile of the T_1 estimates, table 3.5 summarizes T_1 mean and standard deviation for the DESPOT method and the TGV^2_{frob}-regularized MBR approach. For a comparison to the averaged case see figure 3.2 and table 3.3.

Since the TGV^2_{frob} regularised algorithm showed the best performance, further analysis focused on this method.

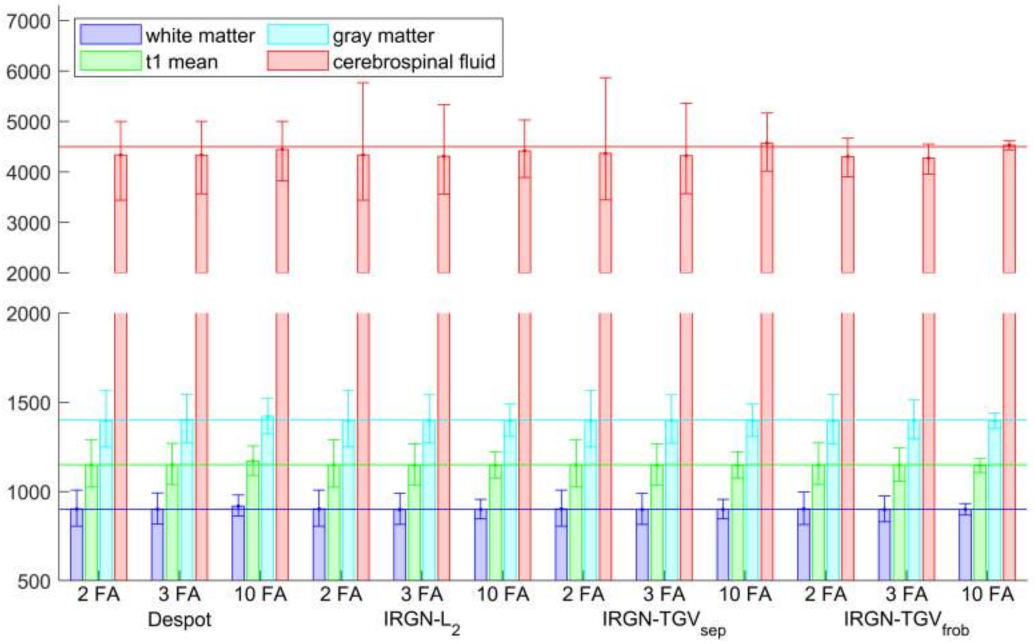

Figure 3.4: Performance of the proposed T_1 mapping methods at a SNR of 15 dB. Median, first and third quartile of T_1 estimates for the four ROIs of the brain grid phantom. T_A varied according to size of the FA sets.

Table 3.5: Performance of the DESPOT method and the TGV^2_{frob}-regularized MBR approach at a SNR of 15 dB. Mean ± standard deviation of T_1 estimates for the four ROIs of the brain grid phantom. T_A varied according to size of the FA sets.

	WM	$T_{1,mean}$	GM	CSF
Reference	900	1150	1400	4500
Despot				
2 FA	912 ± 154	1166 ± 202	1421 ± 248	4147 ± 866
3 FA	908 ± 133	1160 ± 174	1416 ± 207	4198 ± 785
10 FA	923 ± 90	1177 ± 123	1429 ± 151	4325 ± 662
$\boldsymbol{TGV_{frob}}$				
2 FA	910 ± 140	1161 ± 180	1413 ± 215	4251 ± 617
3 FA	904 ± 113	1154 ± 144	1407 ± 169	4237 ± 490
10 FA	900 ± 52	1147 ± 63	1396 ± 69	4512 ± 166

3.1.3 Accelerated T_1 Mapping

Prior to testing the acceleration potential of T_1 quantification methods with in vivo data, by actually creating subsampled data, the outcome was simulated with the brain phantom. Subsampled images were generated by adapting their SNR level based on the hypothetical AF, so that the new SNR level was calculated by $\frac{SNR}{\sqrt{AF}}$. The AFs were chosen to match the ones used for analysis of the vivo data.

Figure 3.5 shows from left to right, the T_1 map used to generate the image data, also representing the ground truth, a T_1 map, reconstructed with the TGV_{frob}^2-regularized MBR approach from fully sampled image data, and the mask used for ROI-based evaluation applied to the fully sampled T_1-map.

Figure 3.6 shows the reconstructed T_1 maps of the numerical brain phantom for the six hypothetical AFs. Figure 3.7 visualizes the results within each ROI by showing the median, as well as the first and third quartile of the T_1 estimates, while table 3.6 lists the mean and standard deviation of the estimated T_1 values.

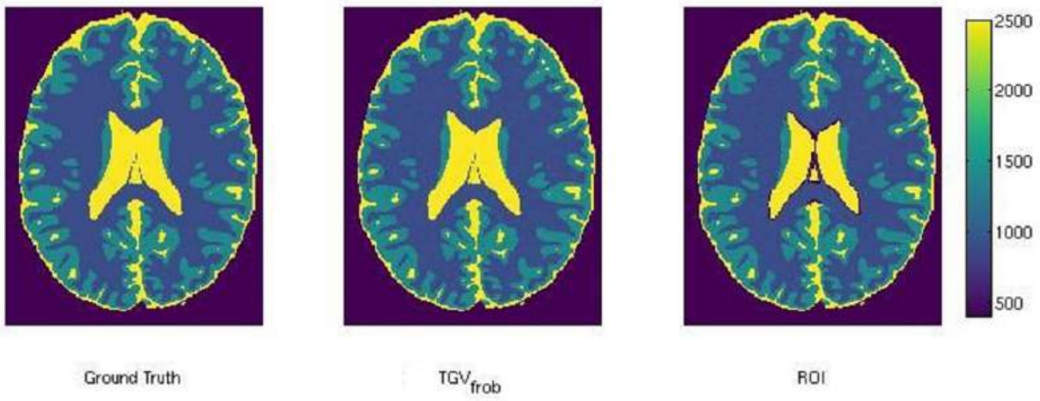

Ground Truth

TGV_{frob}

ROI

Figure 3.5: Reference T_1 map (left), IRGN-TGV_{frob}^2-regularized *image-space* based T_1 reconstruction from fully sampled data (middle) and mask used for ROI-based evaluation (right) of the numerical brain phantom, the ROIs being WM, GM, CSF.

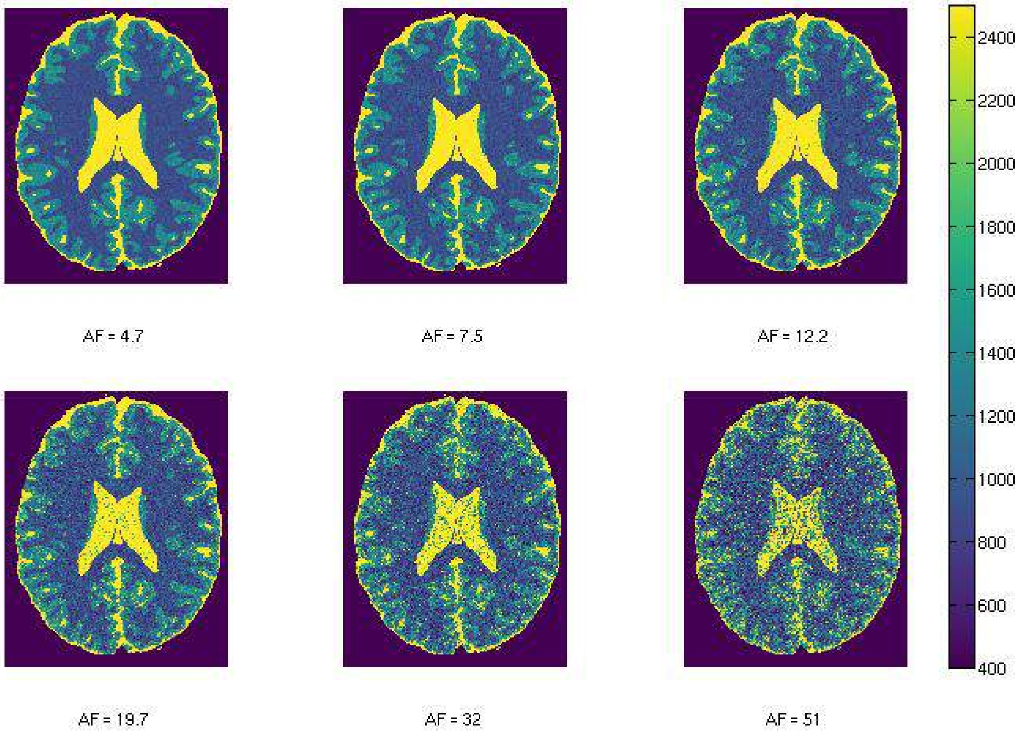

Figure 3.6: $IRGN - TGV^2_{frob}$ regularized *image-space* based T_1 reconstructions of the numerical brain phantom, for six AFs.

Table 3.6: Mean ± standard deviation of T_1 estimates for the three ROIs of the numerical brain phantom, evaluated for fully sampled data and six AFs.

AF	WM	GM	CSF
Ref	900	1400	4500
Full	902 ± 33	1398 ± 50	4209 ± 379
4.7	906 ± 102	1400 ± 156	4086 ± 557
7.5	909 ± 125	1401 ± 191	3944 ± 645
12.2	912 ± 165	1406 ± 253	3830 ± 829
19.7	925 ± 239	1409 ± 364	3497 ± 1065
32	940 ± 300	1415 ± 461	3238 ± 1320
51	974 ± 430	1433 ± 607	2810 ± 1566

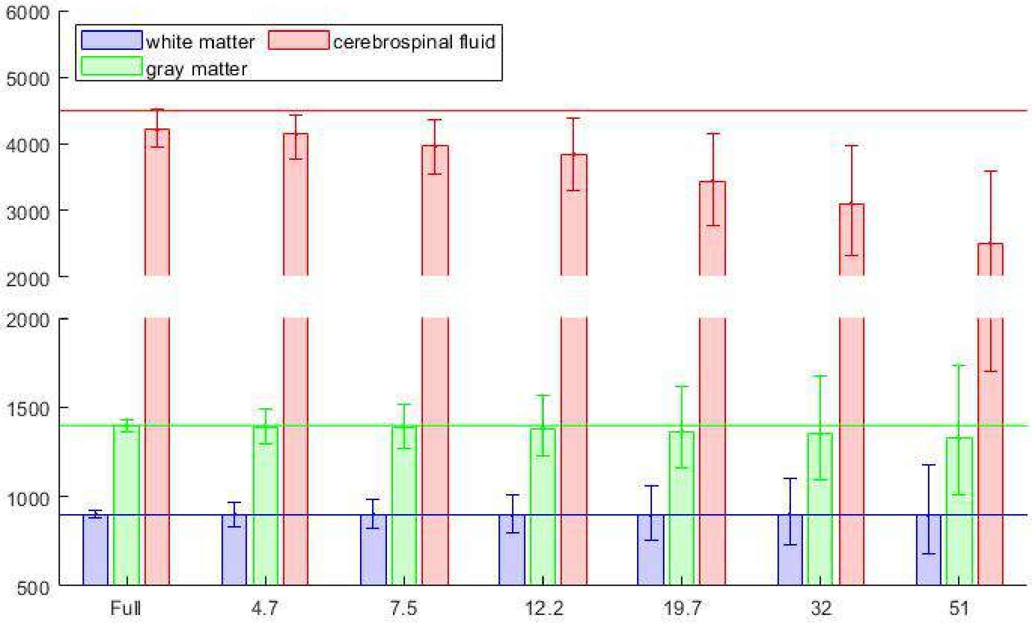

Figure 3.7: Median, first and third quartile of T_1 estimates for the three ROIs of the numerical brain phantom, evaluated for fully sampled data and six AFs.

3.2 In Vivo Brain Measurements

In vivo brain data of three health male volunteers was recorded as described in section 2.2.4, a summary of the scanning parameters is given in table 2.2. T_1 maps were generated with the described MBR reconstruction methods, under usage of TGV^2_{frob} regularization. T_1 quantification was performed directly on the k-space data, as well as on image data, obtained by ICTGV reconstruction, see section 2.2.2. T_1 maps, reconstructed from fully sampled image data, served as a reference when analyzing the acceleration potential of T_1 quantification, and can be found in figures 3.8 to 3.10, for volunteer 1-3 respectively. Images on the right side of figures 3.8 to 3.10 show the masks used for the ROI-based evaluation of estimated T_1 values.

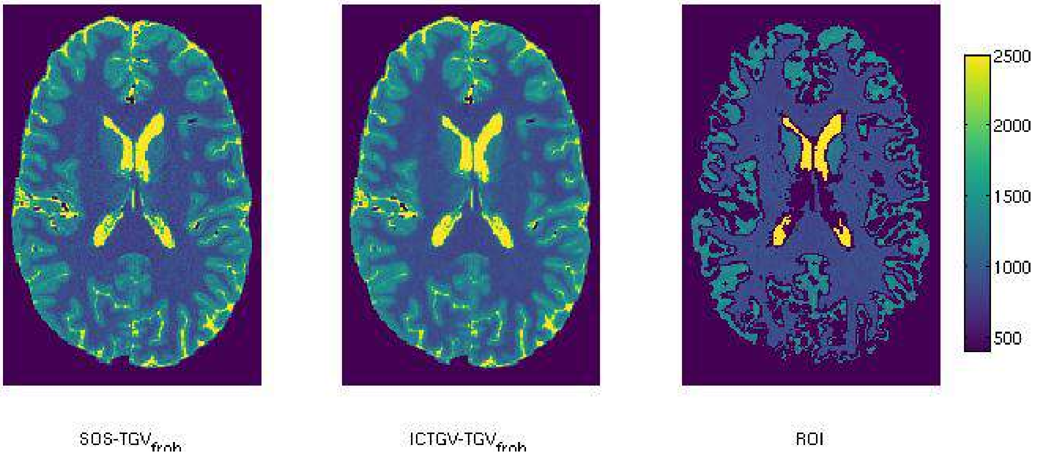

SOS-TGV$_{frob}$ ICTGV-TGV$_{frob}$ ROI

Figure 3.8: $IRGN - TGV^2_{frob}$ regularized *image-space* based T_1 reconstructions of fully sampled in vivo data from volunteer 1. In the left image SOS was used for image reconstruction, while ICTGV was used in the middle image. The right image shows the mask used for ROI-based evaluation, the ROIs being WM, GM, CN and CSF.

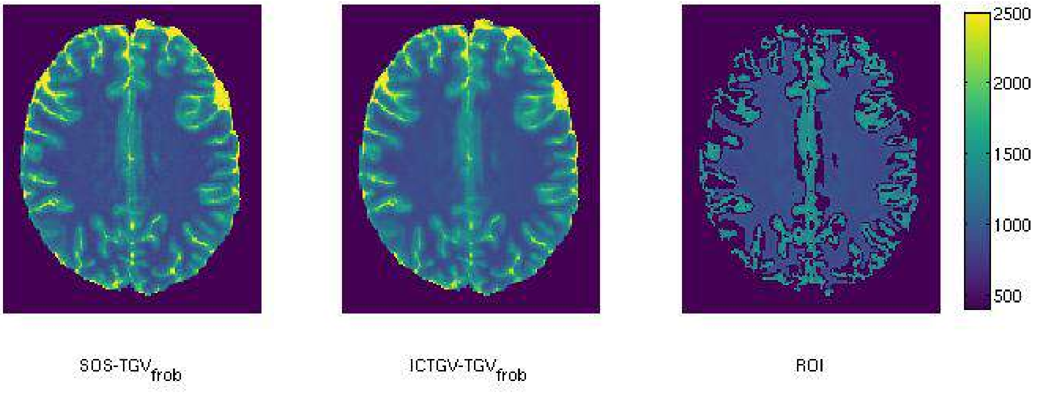

SOS-TGV$_{frob}$ ICTGV-TGV$_{frob}$ ROI

Figure 3.9: $IRGN - TGV^2_{frob}$ regularized *image-space* based T_1 reconstructions of fully sampled in vivo data from volunteer 2. In the left image SOS was used for image reconstruction, while ICTGV was used in the middle image. The right image shows the mask used for ROI-based evaluation, the ROIs being WM and GM.

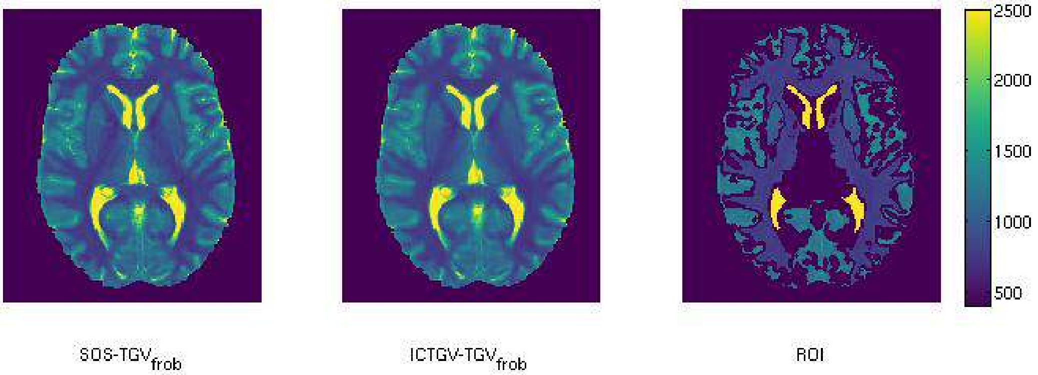

Figure 3.10: $IRGN - TGV^2_{frob}$ regularized *image-space* based T_1 reconstructions of fully sampled in vivo data from volunteer 3. In the left image SOS was used for image reconstruction, while ICTGV was used in the middle image. The right image shows the mask used for ROI-based evaluation, the ROIs being WM, GM, P and CSF.

3.2.1 SNR Stability

Different SNR levels in the vivo data were generated by recording the data using a different slice thickness for each of the three subjects, while the in-plane resolution was kept constant at 1 mm^2. Slice thicknesses used were 1, 3 and 5 mm, for volunteer 1, 2 and 3 respectively. T_1 quantification was performed as described and analogue for each volunteer. Fully sampled T_1 maps were generated from image data only, results can be found in section 3.2. T_1 maps from subsampled data were generated from k-space and ICTGV reconstructed image data, for all three volunteers, i.e. SNR levels. For the sake of clarity all results for accelerated T_1 mapping are presented in section 3.2.2.

3.2.2 Accelerated T_1 Mapping

To test the acceleration potential of the proposed T_1 quantification methods, subsampled data was generated by reducing the number of SPF. The numbers were drawn from the Fibonacci series, starting with 55 SPF, only five SPF were used in the highest subsampling case. All together six AF were evaluated, they are summarised with their corresponding SPF in table 2.3.

To further allow for a direct comparison between T_1 quantification from k-space data, and from ICTGV reconstructed image data, the results are grouped by subjects. All results in this section were generated using the full ten angle sets, see table 2.2. Results for smaller FA sets are presented in section 3.2.2.1.

Reconstructed T_1 maps for volunteer 1 can be found in figure 3.11 for image-space, and figure 3.12 for k-space based T_1 quantification. T_1 estimates are evaluated within four ROIs (WM, GM, P and CSF). Figure 3.13 shows the median and the 25% and 75% percentile, i.e. the first and third quartile of the T_1 estimates, table 3.7 summarizes mean and standard deviation of the estimated T_1 values, for the T_1 maps in figure 3.11. The same evaluation was performed on the T_1 maps from figure 3.12, the results are found in figure 3.14 and table 3.8.

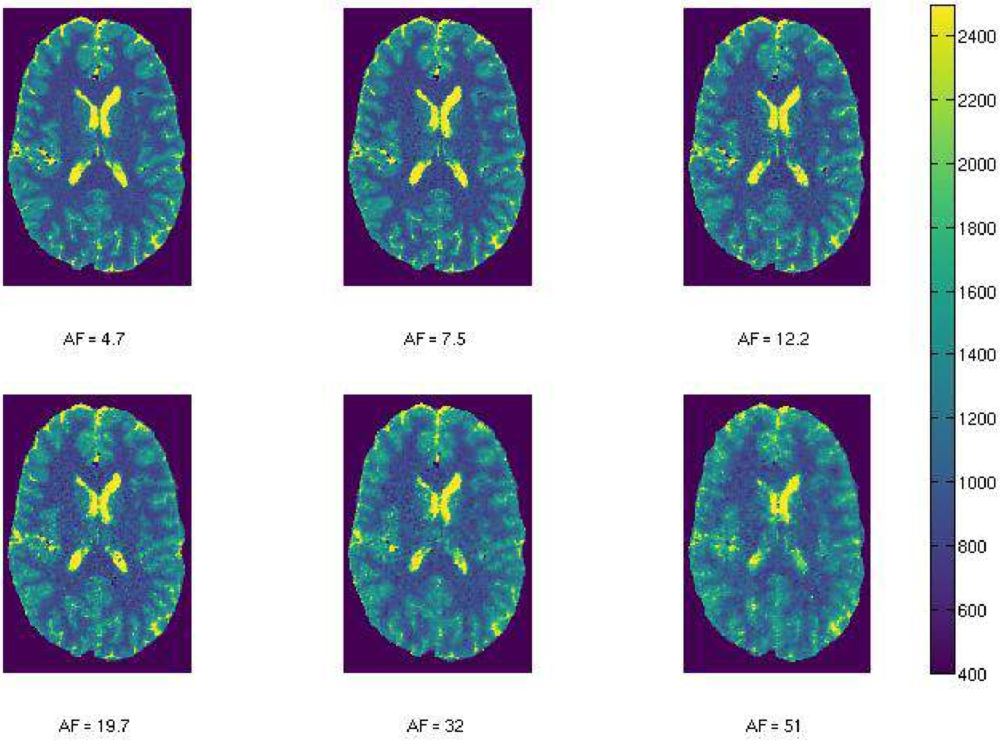

Figure 3.11: Acceleration potential of the $IRGN-TGV_{frob}^2$ regularized *image-space* based T_1 reconstruction. T_1 maps of the in vivo data from volunteer 1 for six AFs. Scanning parameters according to table 2.2.

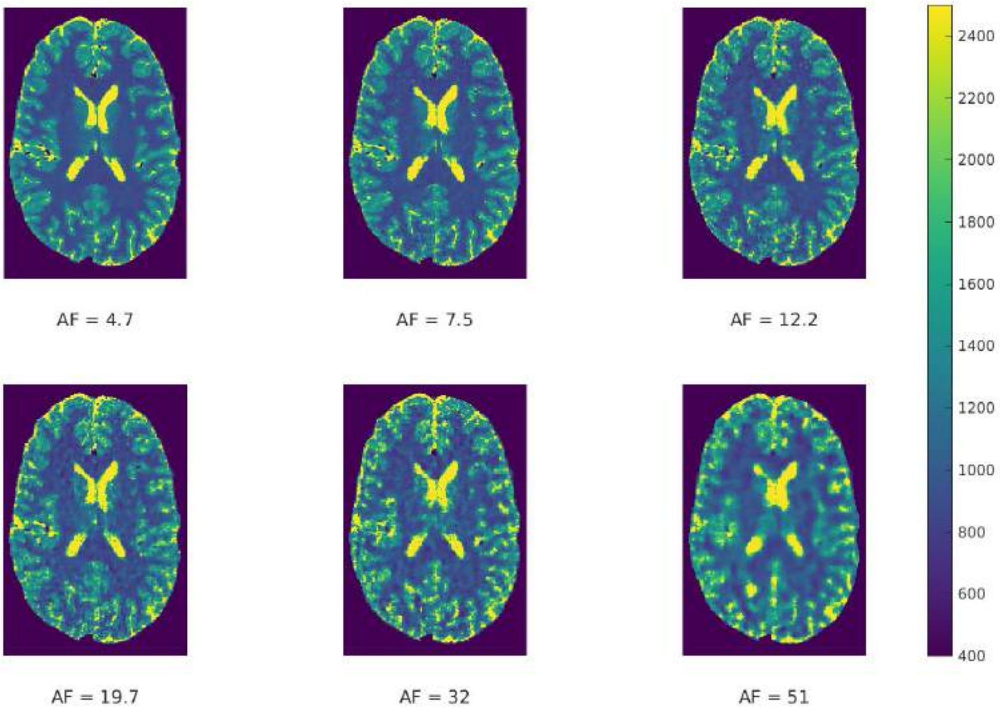

Figure 3.12: Acceleration potential of the $IRGN - TGV^2_{frob}$ regularized *k-space* based T_1 reconstruction. T_1 maps of the in vivo data from volunteer 1 for six AFs. Scanning parameters according to table 2.2.

Table 3.7: Acceleration potential of the $IRGN - TGV^2_{frob}$ regularized *image-space* based T_1 reconstruction. Mean ± standard deviation of T_1 estimates for the four ROIs of the in vivo data of volunteer 1. Six AFs are evaluated, a fully sampled reconstruction serves as reference.

AF	WM	GM	CN	CSF
Full	891 ± 48	1353 ± 100	1195 ± 89	3690 ± 354
4.7	898 ± 86	1357 ± 131	1214 ± 139	3227 ± 384
7.5	904 ± 105	1366 ± 143	1204 ± 192	3306 ± 466
12.2	912 ± 122	1375 ± 160	1206 ± 204	3129 ± 529
19.7	926 ± 130	1388 ± 168	1247 ± 193	3067 ± 503
32	952 ± 129	1405 ± 181	1343 ± 237	2769 ± 505
51	994 ± 145	1417 ± 190	1301 ± 239	2612 ± 641

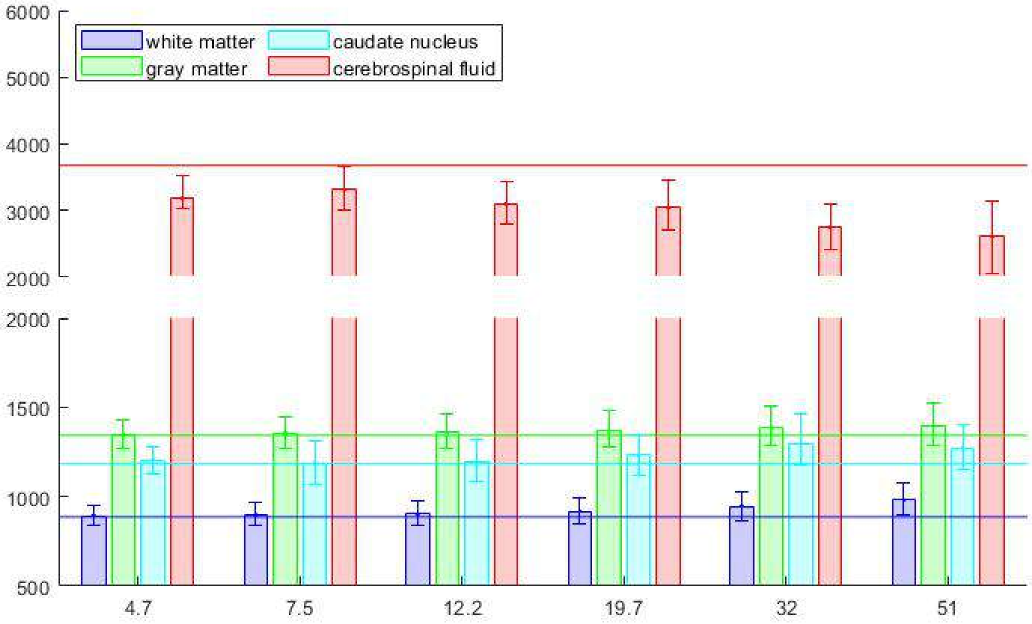

Figure 3.13: Acceleration potential of the $IRGN-TGV^2_{frob}$ regularized *image-space* based T_1 reconstruction. Median, first and third quartile of T_1 estimates for the four ROIs of the in vivo data of volunteer 1. Six AFs are evaluated. The T_1 median of a fully sampled reconstruction serves as reference.

Table 3.8: Acceleration potential of the $IRGN - TGV^2_{frob}$ regularized *k-space* based T_1 reconstruction. Mean ± standard deviation of T_1 estimates for the four ROIs of the in vivo data of volunteer 1. Six AFs are evaluated, a fully sampled reconstruction serves as reference.

AF	WM	GM	CN	CSF
Full	891 ± 48	1353 ± 100	1195 ± 89	3690 ± 354
4.7	910 ± 59	1402 ± 153	1229 ± 99	4190 ± 661
7.5	913 ± 82	1420 ± 194	1237 ± 157	4223 ± 821
12.2	915 ± 99	1434 ± 229	1228 ± 167	3895 ± 896
19.7	927 ± 118	1455 ± 262	1284 ± 313	4111 ± 1004
32	937 ± 137	1539 ± 398	1334 ± 271	4172 ± 1126
51	982 ± 145	1553 ± 345	1275 ± 331	4145 ± 1194

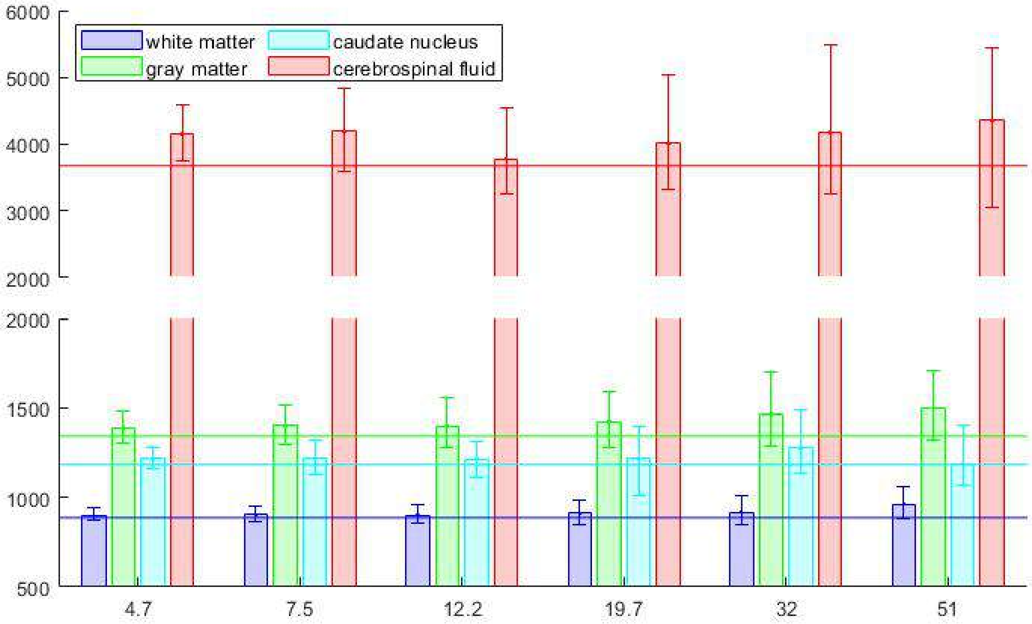

Figure 3.14: Acceleration potential of the $IRGN - TGV^2_{frob}$ regularized *k-space* based T_1 reconstruction. Median, first and third quartile of T_1 estimates for the four ROIs of the in vivo data of volunteer 1. Six AFs are evaluated. The T_1 median of a fully sampled reconstruction serves as reference.

Reconstructed T_1 maps for volunteer 2 can be found in figure 3.15 for image-space, and figure 3.17 for k-space based T_1 quantification. T_1 estimates are evaluated within two ROIs (WM, GM). Figure 3.16 shows the median and the 25% and 75% percentile, i.e. the first and third quartile of the T_1 estimates, table 3.9 summarizes mean and standard deviation of the estimated T_1 values, for the T_1 maps in figure 3.15. The same evaluation was performed on the T_1 maps from figure 3.17, the results are found in figure 3.18 and table 3.10.

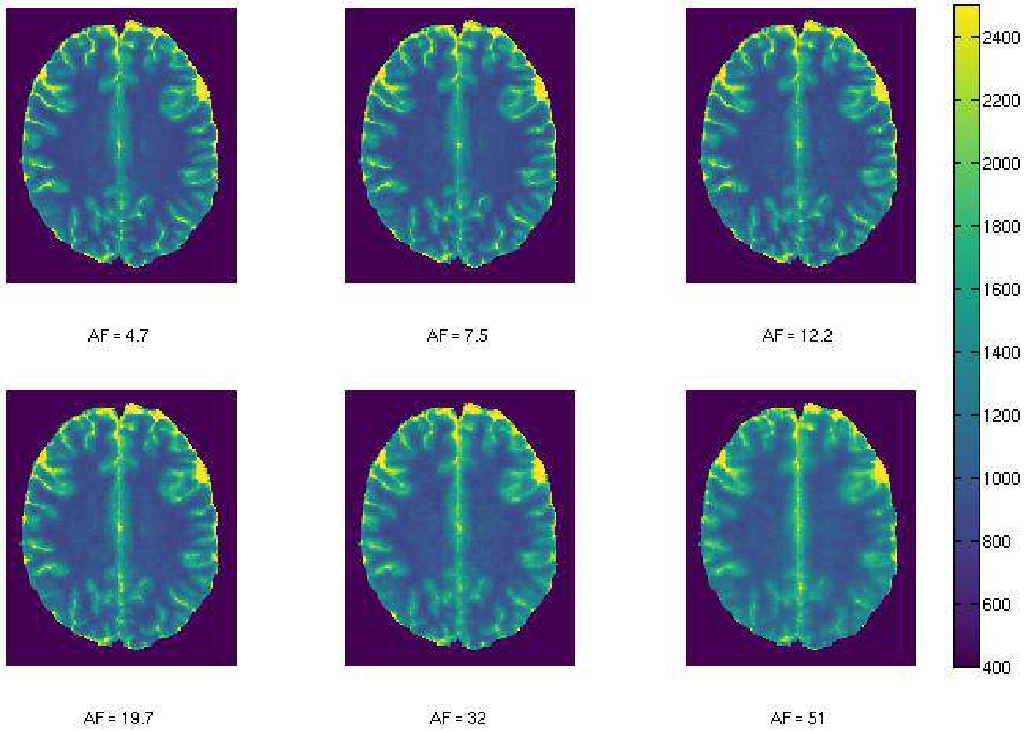

Figure 3.15: Acceleration potential of the $IRGN-TGV^2_{frob}$ regularized *image-space* based T_1 reconstruction. T_1 maps of the in vivo data from volunteer 2 for six AFs. Scanning parameters according to table 2.2, under usage of the ten angle set.

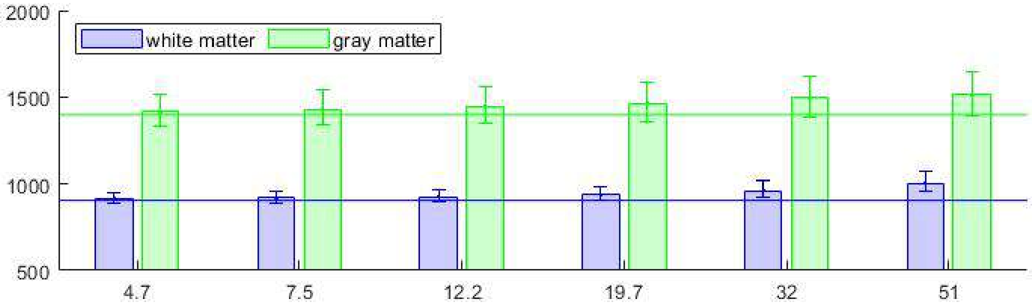

Figure 3.16: Acceleration potential of the $IRGN-TGV^2_{frob}$ regularized *image-space* based T_1 reconstruction. Median, first and third quartile of T_1 estimates for the two ROIs of the in vivo data of volunteer 2, under usage of the ten angle set. Six AFs are evaluated. The T_1 median of a fully sampled reconstruction serves as reference.

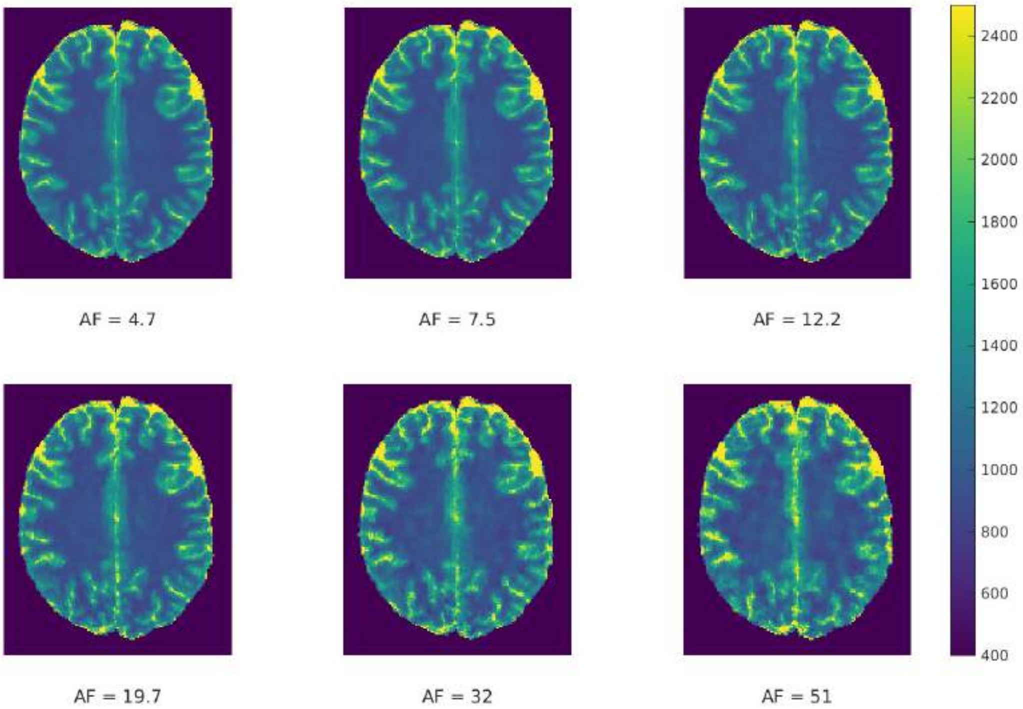

Figure 3.17: Acceleration potential of the $IRGN - TGV^2_{frob}$ regularized *k-space* based T_1 reconstruction. T_1 maps of the in vivo data from volunteer 2 for six AFs. Scanning parameters according to table 2.2, under usage of the ten angle set.

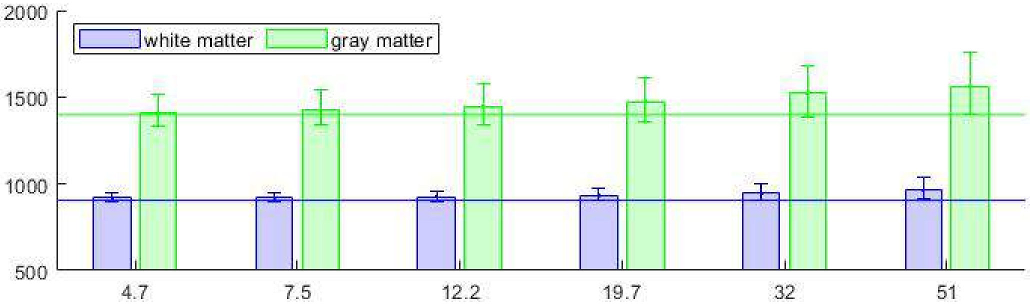

Figure 3.18: Acceleration potential of the $IRGN - TGV^2_{frob}$ regularized *k-space* based T_1 reconstruction. Median, first and third quartile of T_1 estimates for the two ROIs of the in vivo data of volunteer 2, under usage of the ten angle set. Six AFs are evaluated. The T_1 median of a fully sampled reconstruction serves as reference.

Table 3.9: Acceleration potential of the $IRGN - TGV^2_{frob}$ regularized *image-space* based T_1 reconstruction. Mean ± standard deviation of T_1 estimates for the two ROIs of the in vivo data of volunteer 2, under usage of the ten angle set. Six AFs are evaluated, a fully sampled reconstruction serves as reference.

AF	WM	GM
Full	913 ± 44	1418 ± 118
4.7	923 ± 51	1432 ± 127
7.5	928 ± 53	1446 ± 137
12.2	935 ± 58	1464 ± 149
19.7	949 ± 63	1485 ± 164
32	975 ± 74	1513 ± 177
51	1022 ± 88	1533 ± 194

Table 3.10: Acceleration potential of the $IRGN - TGV^2_{frob}$ regularized *k-space* based T_1 reconstruction. Mean ± standard deviation of T_1 estimates for the two ROIs of the in vivo data of volunteer 2, under usage of the ten angle set. Six AFs are evaluated, a fully sampled reconstruction serves as reference.

AF	WM	GM
Full	913 ± 44	1418 ± 118
4.7	930 ± 44	1424 ± 168
7.5	932 ± 48	1444 ± 193
12.2	936 ± 55	1465 ± 206
19.7	943 ± 62	1492 ± 230
32	959 ± 78	1541 ± 267
51	984 ± 102	1602 ± 338

Reconstructed T_1 maps for volunteer 3 can be found in figure 3.19 for image-space, and figure 3.20 for k-space based T_1 quantification. T_1 estimates are evaluated within four ROIs (WM, GM, CN and CSF). Figure 3.21 shows the median and the 25% and 75% percentile, i.e. the first and third quartile of the T_1 estimates, table 3.11 summarizes mean and standard deviation of the estimated T_1 values, for the T_1 maps in figure 3.19. The same evaluation was performed on the T_1 maps from figure 3.20, the results are found in figure 3.22 and table 3.12.

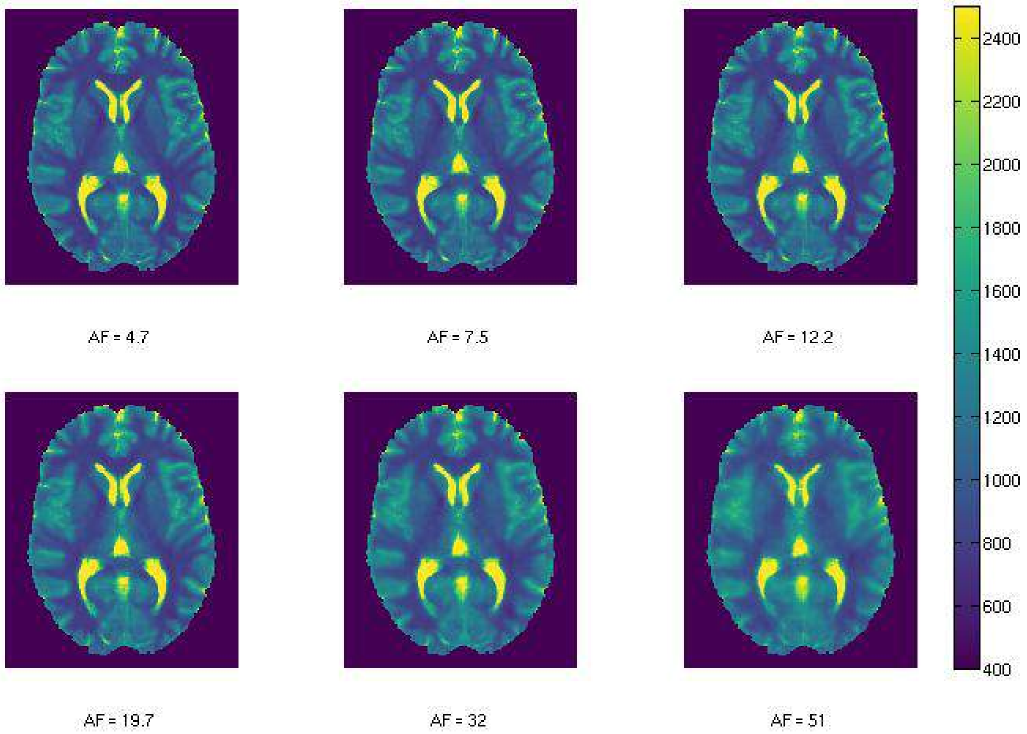

Figure 3.19: Acceleration potential of the $IRGN-TGV^2_{frob}$ regularized *image-space* based T_1 reconstruction. T_1 maps of the in vivo data from volunteer 3 for six AFs. Scanning parameters according to table 2.2.

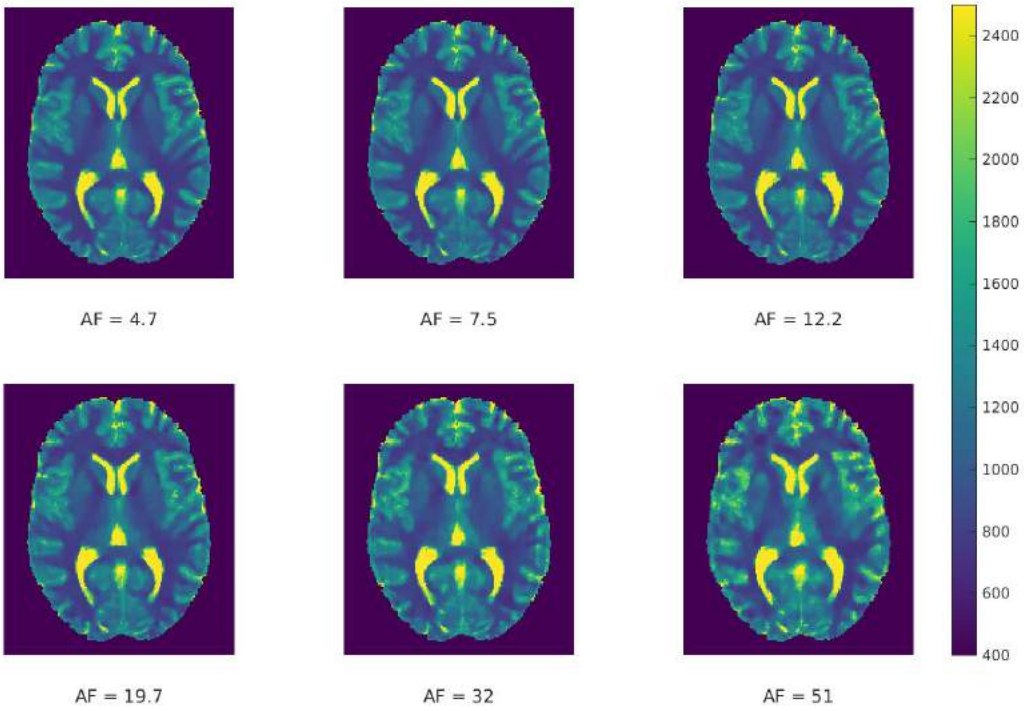

Figure 3.20: Acceleration potential of the $IRGN - TGV^2_{frob}$ regularized *k-space* based T_1 reconstruction. T_1 maps of the in vivo data from volunteer 3 for six AFs. Scanning parameters according to table 2.2.

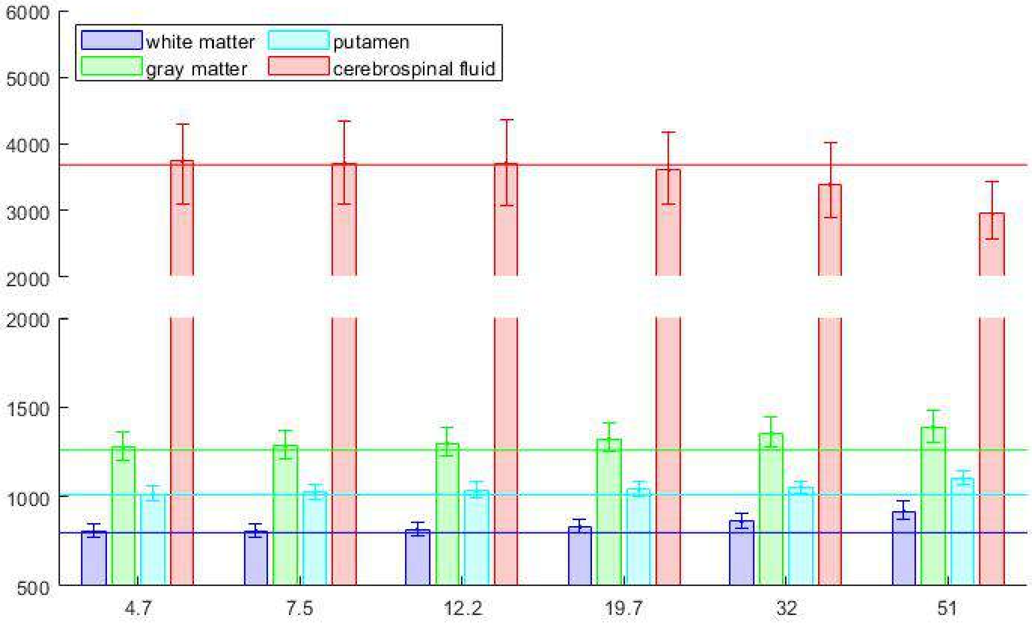

Figure 3.21: Acceleration potential of the $IRGN-TGV^2_{frob}$ regularized *image-space* based T_1 reconstruction. Median, first and third quartile of T_1 estimates for the four ROIs of the in vivo data of volunteer 3. Six AFs are evaluated. The T_1 median of a fully sampled reconstruction serves as reference.

Table 3.11: Acceleration potential of the $IRGN-TGV^2_{frob}$ regularized *image-space* based T_1 reconstruction. Mean ± standard deviation of T_1 estimates for the four ROIs of the in vivo data of volunteer 3. Six AFs are evaluated, a fully sampled reconstruction serves as reference.

AF	WM	GM	P	CSF
Full	804 ± 46	1275 ± 108	1015 ± 52	3728 ± 763
4.7	811 ± 49	1288 ± 110	1023 ± 54	3747 ± 767
7.5	815 ± 51	1297 ± 112	1030 ± 56	3741 ± 781
12.2	822 ± 54	1311 ± 111	1038 ± 59	3752 ± 791
19.7	840 ± 59	1336 ± 112	1045 ± 55	3661 ± 774
32	870 ± 67	1369 ± 117	1054 ± 52	3465 ± 751
51	927 ± 77	1399 ± 128	1103 ± 55	3003 ± 609

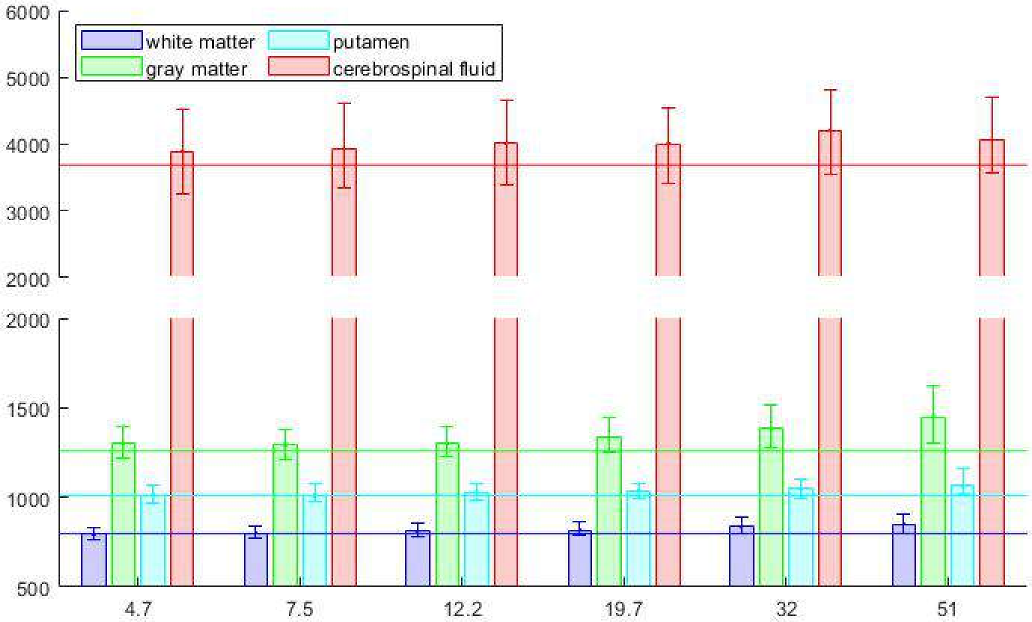

Figure 3.22: Acceleration potential of the $IRGN - TGV^2_{frob}$ regularized *k-space* based T_1 reconstruction. Median, first and third quartile of T_1 estimates for the four ROIs of the in vivo data of volunteer 3. Six AFs are evaluated. The T_1 median of a fully sampled reconstruction serves as reference.

Table 3.12: Acceleration potential of the $IRGN - TGV^2_{frob}$ regularized *k-space* based T_1 reconstruction. Mean ± standard deviation of T_1 estimates for the four ROIs of the in vivo data of volunteer 3. Six AFs are evaluated, a fully sampled reconstruction serves as reference.

AF	WM	GM	P	CSF
Full	804 ± 46	1275 ± 108	1015 ± 52	3728 ± 763
4.7	802 ± 46	1313 ± 124	1019 ± 56	3882 ± 755
7.5	807 ± 46	1307 ± 122	1027 ± 60	3950 ± 764
12.2	821 ± 50	1318 ± 125	1032 ± 56	4034 ± 778
19.7	828 ± 55	1353 ± 143	1040 ± 53	4017 ± 754
32	848 ± 69	1406 ± 191	1053 ± 69	4185 ± 820
51	863 ± 97	1482 ± 254	1105 ± 123	4144 ± 776

3.2.2.1 Model-based Reconstruction in k-Space

While the image-space based T_1 quantification is restricted to large FA sets by the used image reconstruction method, basing the T_1 quantification on k-space data allows for usage of smaller flip angle sets. For comparison of the performance for different numbers of FAs, three FA subsets were defined and volunteer 2 was chosen for evaluation. The acceleration potential of T_1 quantification, was tested for all FA sets. Evaluation of the results was performed as described in section 3.2.2 for the ten angle sets.

Reconstructed T_1 maps for the flip angle set $\{2°, 14°, 17°\}$ can be found in figure 3.23, figure 3.24 shows the median and the 25% and 75% percentile, i.e. the first and third quartile of the T_1 estimates, evaluated within the two ROIs (WM, GM).

Reconstructed T_1 maps for the flip angle set $\{2°, 14°, 14°\}$ can be found in figure 3.25, figure 3.26 shows the median and the 25% and 75% percentile, i.e. the first and third quartile of the T_1 estimates.

Reconstructed T_1 maps for the flip angle set $\{2°, 14°\}$ can be found in figure 3.27, figure 3.28 shows the median and the 25% and 75% percentile, i.e. the first and third quartile of the T_1 estimates.

Table 3.13 finally summarizes mean and standard deviation of the estimated T_1 values, for all three used FA subsets.

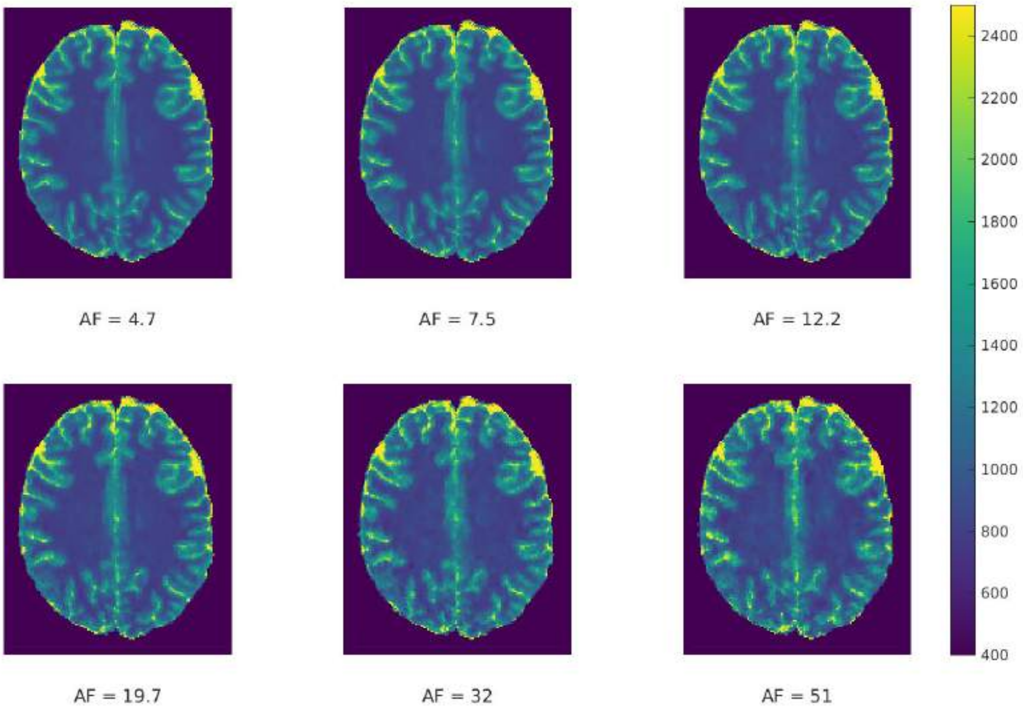

Figure 3.23: Acceleration potential of the $IRGN - TGV^2_{frob}$ regularized *k-space* based T_1 reconstruction. T_1 maps of the in vivo data from volunteer 2 for six AFs. Scanning parameters according to table 2.2, under usage of the three angle set $\{2°, 14°, 17°\}$.

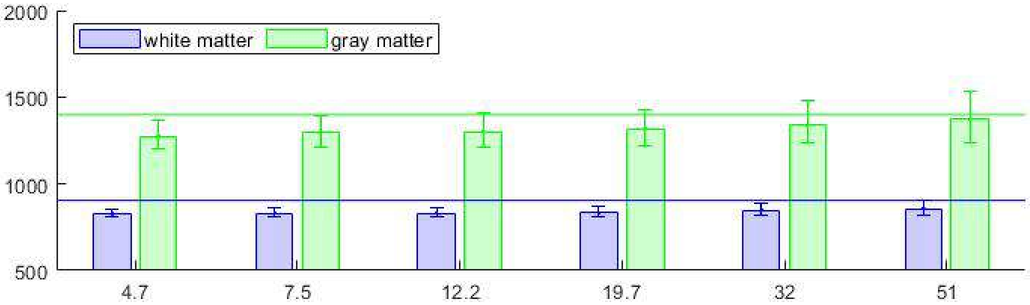

Figure 3.24: Acceleration potential of the $IRGN - TGV^2_{frob}$ regularized *k-space* based T_1 reconstruction. Median, first and third quartile of T_1 estimates for the two ROIs of the in vivo data of volunteer 2, under usage of the three angle set $\{2°, 14°, 17°\}$. Six AFs are evaluated. The T_1 median of a fully sampled reconstruction serves as reference.

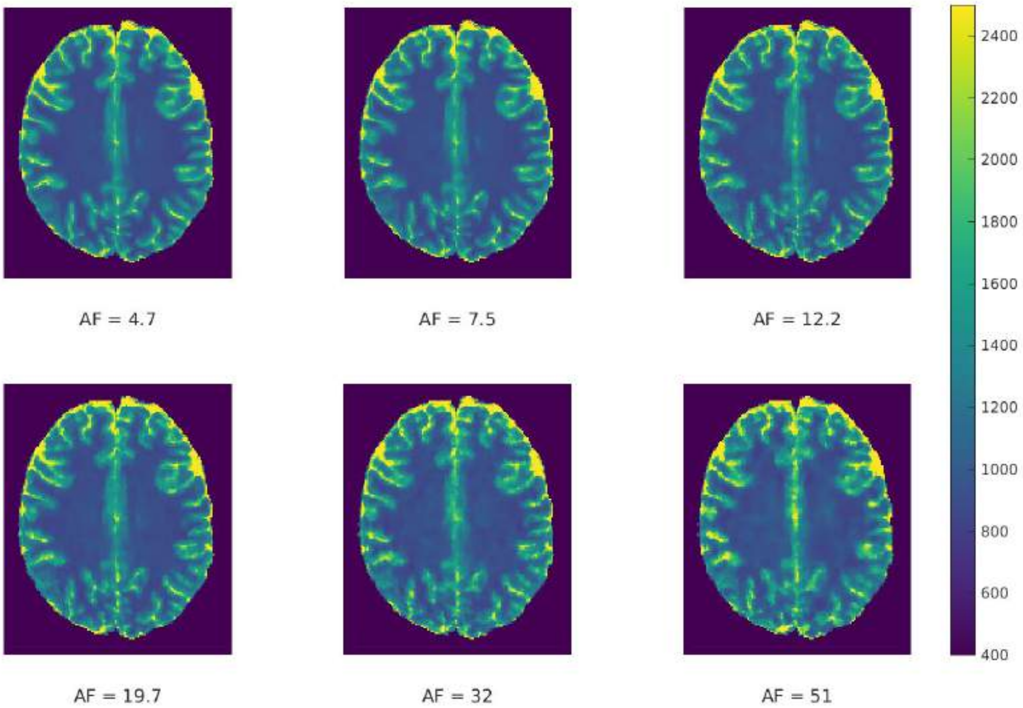

Figure 3.25: Acceleration potential of the $IRGN - TGV^2_{frob}$ regularized *k-space* based T_1 reconstruction. T_1 maps of the in vivo data from volunteer 2 for six AFs. Scanning parameters according to table 2.2, under usage of the three angle set $\{2°, 14°, 14°\}$.

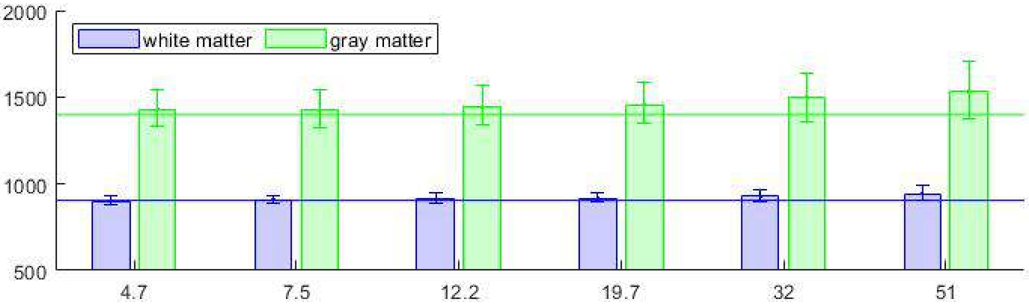

Figure 3.26: Acceleration potential of the $IRGN - TGV^2_{frob}$ regularized *k-space* based T_1 reconstruction. Median, first and third quartile of T_1 estimates for the two ROIs of the in vivo data of volunteer 2, under usage of the three angle set $\{2°, 14°, 14°\}$. Six AFs are evaluated. The T_1 median of a fully sampled reconstruction serves as reference.

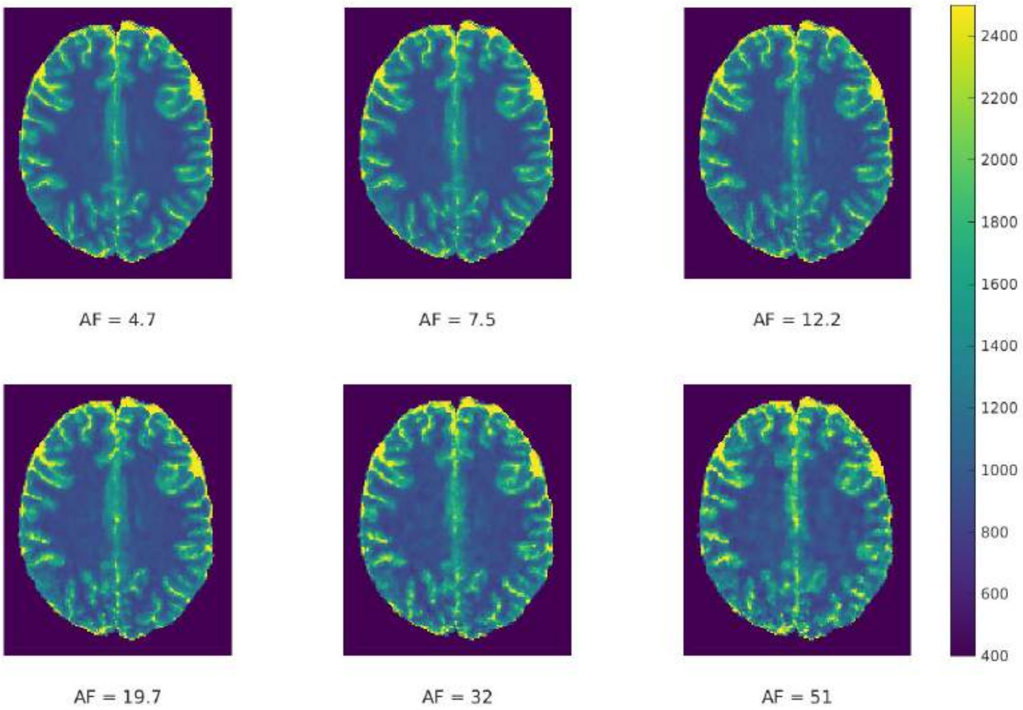

Figure 3.27: Acceleration potential of the $IRGN - TGV^2_{frob}$ regularized *k-space* based T_1 reconstruction. T_1 maps of the in vivo data from volunteer 2 for six AFs. Scanning parameters according to table 2.2, under usage of the two angle set $\{2°, 14°\}$.

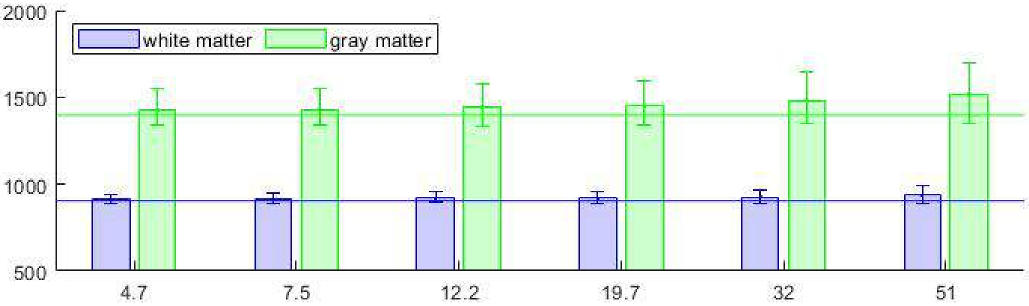

Figure 3.28: Acceleration potential of the $IRGN - TGV^2_{frob}$ regularized *k-space* based T_1 reconstruction. Median, first and third quartile of T_1 estimates for the two ROIs of the in vivo data of volunteer 2, under usage of the two angle set $\{2°, 14°\}$. Six AFs are evaluated. The T_1 median of a fully sampled reconstruction serves as reference.

Table 3.13: Acceleration potential of the $IRGN - TGV^2_{frob}$ regularized *k-space* based T_1 reconstruction. Mean ± standard deviation of T_1 estimates for the two ROIs of the in vivo data of volunteer 2, under usage of the two three angle sets and the two angle set. Six AFs are evaluated, a fully sampled reconstruction serves as reference.

	3 FA $\{2°, 14°, 17°\}$		**3 FA** $\{2°, 14°, 14°\}$		**2 FA** $\{2°, 14°\}$	
AF	WM	GM	WM	GM	WM	GM
Full	913 ± 44	1418 ± 118				
4.7	837 ± 44	1287 ± 157	913 ± 46	1447 ± 151	922 ± 52	1447 ± 224
7.5	839 ± 46	1302 ± 164	918 ± 47	1444 ± 161	925 ± 54	1447 ± 192
12.2	842 ± 50	1312 ± 177	925 ± 53	1464 ± 178	930 ± 58	1462 ± 212
19.7	846 ± 55	1331 ± 194	931 ± 58	1483 ± 200	932 ± 62	1472 ± 228
32	857 ± 64	1360 ± 226	943 ± 67	1520 ± 242	936 ± 71	1506 ± 270
51	871 ± 80	1397 ± 259	958 ± 83	1562 ± 282	952 ± 89	1543 ± 315

4 Discussion and Conclusion

4.1 Numerical Simulations

To examine noise dependency on the performance of the proposed T_1 quantification methods three SNR levels were simulated with the numerical grid phantom. The highest included SNR level was 30 dB, which roughly equates to levels present in in vivo data with a 1 mm^2 in-plane resolution and a slice thickness of 3mm, i.e. the level measured at the Ernst angle of volunteer 2 image data. No significant improvement of T_1 accuracy or major differences between proposed methods were observed for SNR levels higher than 30 dB and respective results were excluded from the work.

Figures 3.1 to 3.3 show that the performance of IRGN methods does not depend too much on the different implemented regularization strategies. All three yielded similiar results in terms of median T_1 and their behaviour over different flip angles sets. TGV^2_{frob} regularization however, yielded the best results in terms of T_1 accuracy, which can be seen by the much smaller interquartile range.

Reconstructions with the DESPOT method were generally in good agreement with reference values but showed an overestimation in regions with low to medium T_1 values, i.e. WM, $T_{1,mean}$ and GM and an underestimation of CSF T_1 values, when using the ten angle set. Described bias can be observed at 15 dB, and is even more pronounced at 5 dB, where it was also slightly present in the three angle set reconstructions. Its absence in the high

SNR case and the later (3 FA), respectively missing (2 FA) onset in the small flip angle sets, exhibiting improved SNR due to averaging, shows the dependence of the linearized DESPOT approach on high SNR levels in the individual images. Evaluating 15 dB image data without averaging it for the smaller FA sets shows an underestimation of CSF T_1 values for two and three FAs, while no overestimation of low to median T_1 values was observed. In accordance to this, DESPOT reconstructed mean T_1 values shown in table 3.5 were still more accurate than in the ten angle case. Standard deviation approximately doubled in comparison to averaged data.

In comparison to DESPOT, model-based reconstruction methods showed a higher robustness to different numbers of FAs. In T_1 estimates from TGV^2_{frob} regularized MBR no pronounced differences between FA sets were observed at 30 and 15 dB. However the dual angle set yielded better results in both, DESPOT reconstructions across SNR levels, and MBR reconstructions at the low SNR of 5 dB. While a ten angle set gave the worst results in the DESPOT case, as described above, in MBR it was the three angle that lead to slightly less accurate estimates than the other two sets. Lowering the SNR from 30 to 15 dB, approximately doubles the standard deviation for DESPOT reconstruction. Rise of standard deviation was more pronounced in MBR results, however stayed beneath DESPOT levels over all SNR levels. It is worth mentioning that a perfect adaption of regularization parameters to different SNR levels can not be guaranteed and may account for some of the variations observed. Summarizing it can be said that TGV^2_{frob} regularized MBR exhibited higher accuracy in terms of T_1 mean, and slightly improved standard deviation, down to about two thirds, in comparison to DESPOT, see tables 3.2 to 3.4.

Simulations of accelerated data acquisition in the numerical brain phantom, yielded T_1 maps with visible noise, which increased over AFs, see figure 3.6. Edges and small details are preserved well up to an AF of 12.2, corresponding to 21 spokes. Figure 3.7 shows that median T_1 values were constant over all accelerations for WM, and decreased over AFs for GM and CSF, showing a underestimation of CSF values already present in fully sampled data. Mean T_1 values, listed in table 3.6, in contrast showed a bias towards higher values for GM, which was also observable WM.

After phantom simulations, the acceleration potential of TGV^2_{frob} regularized MBR and its performance under different SNR scenarios were evaluated for in vivo data. The results are discussed in sections 4.2.3 and 4.2.1, respectively. A few differences between the numerical model setup and the actual conditions when using the proposed reconstruction pipeline on in vivo data are worth mentioning. Firstly image reconstruction with ICTGV not only allows for subsampling and therefore accelerates the measurement process, it also denoises the images. This leads to an improved SNR compared to the one calculated for the respective AFs in the numerical brain phantom. The noise removal on the downside can lead to errors in the quantification process, since the assumption of gaussian distributed noise justifiying the use of an L_2-norm may not hold. And second a reduction of the number of FA to values as small as two or three is not feasible for ICTGV reconstruction from VFA data because the reduced number of scans leads to a reduction of coherence over the parametric dimension. As ICTGV was developed for dynamic reconstruction, a certain number of scans is mandatory to achieve good reconstruction results. Since literature on FA selection recommends the use of ten angle sets for correct T_1 estimation over broader ranges, with established sets tuned to brain tissue available [12], this number was set to ten.

4.2 In Vivo Reconstruction

4.2.1 SNR Stability

Comparing mean T_1 and standard deviation of image-space based T_1 reconstructions from fully sampled in vivo data to gold standard IR values in table 2.4, estimates for WM are found to be in good accordance with the reference. Slice thicknesses of 1 and 3 mm yielded values of 891 and 913 respectively, while at a slice thickness of 5mm T_1 had the significantly lower value of 804. Standard deviations were located between 44 and 48, similar to reference. Values for GM were 1353 and 1418 for 1 and 3 mm respectively, being in the range of one standard deviation of the reference value generated at a 5 mm slice thickness. T_1 mean for GM at 5mm finally was 1275. Standard deviations were located between 100 and 118, similar to reference. T_1 mean values of the remaining ROIs (CN, P and CSF) were lower than the reference values. As they were not evaluated in all volunteers no statement regarding their SNR stability can be deduced.

Interestingly the trend of increasing mean T_1 values for decreasing SNR levels found in reference values, and observed in the numerical grid phantom could not be observed over all SNR levels in the in vivo data. While the lowest T_1 values for WM and GM were, as expected, observed for a slice thickness of 5mm, highest values were present at 3 mm, with estimates at 1 mm lying just inbetween. However, different subjects were used to record the data with different slice thicknesses, therefore some observed differences could be accounted for by intersubject variability.

4.2.2 Comparison of Mapping Methods

For testing the acceleration potential, references subject to the same scanning environment had to be generated. An ICTGV image reconstruction of fully sampled data, followed by TGV_{frob}^2 regularized MBR, was used to create reference T_1 estimates for each subject, i.e. slice thickness. While these were in agreement to literature values and considered as ground truth in this work, no further proof was performed by e.g. using another measurement or reconstruction method. No fully sampled T_1 reconstruction was obtained from k-space data. T_1 values reconstructed from k-space data were slightly higher than those reconstructed from image data, but in overall good accordance. The difference, however, did lead to a somewhat higher deviation from the specified reference values when looking at k-space based reconstructions. This is only apparent in the region of low AFs, as the bias introduced over the accelerations quickly disguises the minor difference.

Both methods, MBR on k-space data, as well as the combination of ICTGV image reconstruction and MBR on the resultant image data, yielded T_1 estimates that were in good accordance with literature reference values.

4.2.3 Acceleration Potential

Mean T_1 values estimated from subsampled data showed good compliance with the fully sampled reference values, staying within two standard deviations over all accelerations. Only image-space based reconstructions of WM slightly exceeded that limit for an AF of 51 for volunteer 1 and 2. All reconstructions showed the same overestimation bias for low to medium T_1 values, i.e. within all ROIs except CSF, increasing over accelerations. This is consistent with the observations in the numerical brain phantom, see section 4.1. CSF T_1 values showed a bias towards lower values for increasing accelerations in reconstructions from image data, as observed in the numerical simulations, see figures 3.13 and 3.21 and for corresponding values tables 3.7 and 3.11. In reconstructions from k-space data however, CSF values followed the trend of low to medium T_1 estimates showing a bias to higher values over accelerations, see figures 3.14 and 3.22 and for corresponding values tables 3.8 and 3.12.

Visually high AF factors lead to blurred T_1 maps for image-space based reconstruction, producing unsharp edges and loss of details. k-Space based reconstructed T_1 maps showed a tendency to form subregions of different T_1 within regions of former constant T_1 at high AFs. This results in a patchy image, see for example in figure 3.20 the frontal region at AFs of 32 and 51.

AFs up to 12.2, respectively 19.7, depending on the accepted image degradation led to good visual results. The corresponding mean T_1 values stayed within one standard deviation of the reference. This suggests that T_1 quantification is possible with as little as 21, respectively 13 Spokes per Frame, when using ten FAs, enabling scan time reduction from 12.8 seconds per slice, to 1.05, respectively 0.65 seconds per slice.

A comparison of different sizes of FA sets was performed for volunteer 2. The three angle set of $\{2°, 14°, 17°\}$ was selected by the algorithm as the best subset from a provided ten angle set, not allowing for repetition of angles within the set. While this angle set performed well for DESPOT, it showed the least accurate results within the TGV^2_{frob} regularized MBR on phantom image data, see section 4.1. In case of reconstruction from in vivo k-space data the T_1 quantification, using this angle set, showed severe estimation errors, consistently underestimating T_1 values over all acceleration. Another three FA set was created from repetition of one of the angles of the dual angle set $\{2°, 14°\}$, as suggested by Lewis et al. [10], giving $\{2°, 14°, 14°\}$. Both FA sets gave similarly good results, outperforming the k-space based reconstruction with the ten angle set, see table 3.10 and 3.13. For the region of WM they even outperformed that of the image-space based one, see table 3.9. Overall the triple angle set yielded the best results within k-space based IRGN-TGV^2_{frob} reconstruction, with mean T_1 values in good accordance with the reference value, exhibiting the smallest observed standard deviations.

4.3 Conclusion

The present work analyzes model-based T_1 quantification methods, working on either image or k-space data, in terms of their stability to different scanning scenarios, focusing especially on their acceleration potential. The underlying model was the VFA approach, the proposed algorithms are based on the IRGN method.

Numerical simulation showed a higher robustness to different numbers of FAs and SNR levels for MBR in comparison to DESPOT. Highest T_1 accuracy could be achieved using TGV^2_{frob} regularization.

T_1 reconstructions from in vivo data, were found to be in overall good agreement with literature reference values for both, the combination of ICTGV image reconstruction and MBR on the resultant image data as well as MBR on k-space data, the latter showing slightly higher T_1 values.

Mean T_1 values from subsampled data showed good compliance with the fully sampled reference, staying mostly within two standard deviations over all accelerations. A bias of overestimating low to median T_1 values was observed in both methods, while high T_1 values were underestimated in image-space based reconstructions and overestimated in k-space based reconstructions, biases increased with increasing AFs. Considering the visual results and demanding T_1 values to stay within one standard deviation of the reference the scan time could be reduced from 12.8 seconds per slice to 1.05, respectively 0.65 second per slice depending on the accepted image degradation.

The evaluation of smaller FA sets consisting of two and three angles, performed for k-space based MBR, outperformed the ten angle set in the evaluated regions of WM and GM.

The next step towards a more thorough evaluation of the proposed T_1 quantification methods could be including other signal models apart from the VFA approach.

5 Algorithms

Algorithm 1: Iteratively regularized Gauss-Newton algorithm with different regularization strategies for qMRI

```
Initialize:
$k = 0,\ u_k = (q_1, \cdots, q_{N_q}) = 0, \lambda, \delta, \gamma, q_\delta, q_\gamma$
while $k < N_{max}$ do
    Initialize $DS|_{u=u_k},\ DS^H|_{u=u_k}$
    Compute $\tilde{I}_p = I_p + DS_p u_k - S_p(u_k),\ p = 1, \cdots, N_p$
    Choose regularization strategy:
    if $\mathcal{R}_{L^2}(u)$ then
        Compute $u_{k+1}$ with algorithm 2
    end
    if $\mathcal{R}(u) = TGV^2_{sep}(u)$ then
        Compute $u_{k+1}$ with algorithm 3
    end
    if $\mathcal{R}(u) = TGV^2_{frob}(u)$ then
        Compute $u_{k+1}$ with algorithm 4
    end
    $\delta \leftarrow \delta q_\delta$
    $\gamma \leftarrow \delta q_\delta$
end
```

Algorithm 2: Conjugate Gradient method for L^2 regularized subproblem of algorithm 1 for qMRI in image space.

```
Definitions:
$U = \mathbb{C}^{N_x \times N_y}$

Initialize:
$u \in U^2,\ M = \lambda DS^H DS + (\frac{1}{\tau} + \delta)Id,\ rhs = \lambda DS^H \tilde{I} + \delta u_k$

Solve with CG method
$r_0 = r - Mx_0,\ p_0 = r_0$

while $k < N_{max}$ do
    $\alpha_k = \frac{<r_k,r_k>}{<p_k,Mp_k>}$
    $u^+ \leftarrow u_k + \alpha_k p_k$
    $r^+ \leftarrow r_k + \alpha_k M p_k$

    $\beta_k = \frac{<r^+,r^+>}{<r,r>}$
    $p^+ = r^+ + \beta_k p_k$
end
```

Algorithm 3: Primal-Dual Algorithm for IRGN-TGV^2_{sep} subproblem in image space

```
Definitions:
$U = \mathbb{C}^{N_x \times N_y}$,
$\nabla : U \to U^2,\ \mathcal{E} : U^2 \to U^3$

Initialize:
$\sigma, \tau = \frac{1}{\sqrt{12}},\ u_i, \bar{u}_i \in U,\ v_i, \bar{v}_i \in U^2,\ p_i \in U^2,\ q_i \in U^3,\ i = 1, \cdots, P,$
$M = \lambda DS^H DS + (\frac{1}{\tau} + \delta) Id,\ r_{\text{part}} = \lambda DS^H \tilde{I} + \delta u_k$

while $k < maxit$ do
    Dual Update:
    $p_i^+ \leftarrow P_\gamma \left( p_i + \sigma(\nabla \bar{u}_i - \bar{v}_i) \right)$
    $q_i^+ \leftarrow P_{2\gamma} \left( q_i + \sigma \mathcal{E} \bar{v}_i \right)$

    Primal Update:
    $u_i^+ \leftarrow P_{L^2}(u_i + \tau \text{div}^1 p_i^+)$
    $v_i^+ \leftarrow v - \tau(-p_i^+ - \text{div}^2 q_i^+)$

    Extrapolation and Update:
    $(\bar{u}_i, \bar{v}_i) \leftarrow 2(u_i^+, v_i^+) - (u_i, v_i)$
    $(u_i, v_i) \leftarrow (u_i^+, v_i^+)$
end
```

$$P_\eta(\xi)_{j,l} = \frac{\xi_{j,l}}{\max\left(1, \frac{|\xi_{j,l}|}{\eta}\right)} \quad \text{and} \quad P_{L^2}(\xi) = M^{-1}\left(r_{\text{part}} + \frac{\xi}{\tau} \right)$$

Algorithm 4: Primal-Dual Algorithm for IRGN-TGV^2_{frob} subproblem in image space

```
Definitions:
$U = \mathbb{C}^N,\ N = N_x N_y$, space of vectorized 2D parameter images,
$\nabla : U^P \to U^{P\times 2},\ \mathcal{E} : U^{P\times 2} \to U^{P\times 3}$

Initialize:
$\sigma, \tau = \frac{1}{\sqrt{12}},\ u, \bar{u} \in U^P,\ v, \bar{v} \in U^{P\times 2},\ p \in U^{P\times 2},\ q \in U^{P\times 3},$
$M = \lambda DS^H DS + (\frac{1}{\tau} + \delta) Id,\ r_{\text{part}} = \lambda DS^H \tilde{I} + \delta u_k$

while $k < maxit$ do
    Dual Update:
    $p^+ \leftarrow P_\gamma\left(p + \sigma(\nabla \bar{u} - \bar{v})\right)$
    $q^+ \leftarrow P_{2\gamma}\left(q + \sigma \mathcal{E} \bar{v}\right)$

    Primal Update:
    $u^+ \leftarrow P_{L^2}(u + \tau \text{div}^1 p^+)$
    $v^+ \leftarrow v - \tau(-p^+ - \text{div}^2 q^+)$

    Stepsize Update:
    $\sigma_+ \leftarrow \mathcal{S}\left(\sigma\tau, \frac{\|(u^+,v^+,w_1^+,w_2^+)-(u,v,w_1,w_2)\|}{\|H((u^+,v^+,w_1^+,w_2^+)-(u,v,w_1,w_2))\|}\right)$
    $\tau_+ \leftarrow \sigma_+$

    Extrapolation and Update:
    $(\bar{u}, \bar{v}) \leftarrow 2(u^+, v^+) - (u, v)$
    $(u, v) \leftarrow (u^+, v^+)$
end
```

$$P_\eta(\xi)_{i,p} = \frac{\xi_{i,p}}{\max\left(1, \frac{|\xi|_{\text{frob}}}{\eta}\right)} \quad \text{and} \quad P_{L^2}(\xi) = M^{-1}\left(r_{\text{part}} + \frac{\xi}{\tau}\right)$$

Algorithm 5: Primal-Dual Algorithm for IRGN-TGV^2_{frob} subproblem in k-space

```
Definitions:
$U = \mathbb{C}^N, N = N_x N_y$, space of vectorized 2d parameter images,
$\nabla : U^P \to U^{P\times 2}$, $\mathcal{E} : U^{P\times 2} \to U^{P\times 3}$, $|| \cdot ||_F$ :

Initialize:
$\sigma, \tau = \frac{1}{\sqrt{12}}$ $u, \bar{u} \in U^P$, $v, \bar{v} \in U^{P\times 2}$, $p \in U^{P\times 2}$, $q \in U^{P\times 3}$

while $k < maxit$ do
    Dual Update:
    $p^+ \leftarrow P_\gamma \left(p + \sigma(\nabla\bar{u} - \bar{v})\right)$
    $q^+ \leftarrow P_{\sqrt{2}\gamma} \left(q + \sigma\mathcal{E}\bar{v}\right)$
    $r^+ \to P_{L_2} \left(r + \sigma \left(DG - \tilde{I}\right)\right)$

    Primal Update:
    $u^+ \leftarrow P_{l_2}(u + \tau\mathrm{div}_1 p^+ - DG^H(r^+))$
    $v^+ \leftarrow v - \tau(-p^+ - \mathrm{div}_2 q^+)$

    Stepsize Update:
    $\sigma_+ \leftarrow \mathcal{S}\left(\sigma\tau, \frac{\|(u^+,v^+,w_1^+,w_2^+)-(u,v,w_1,w_2)\|}{\|H((u^+,v^+,w_1^+,w_2^+)-(u,v,w_1,w_2))\|}\right)$
    $\tau_+ \leftarrow \sigma_+$

    Extrapolation and Update:
    $(\bar{u}, \bar{v}) \leftarrow 2(u^+, v^+) - (u, v)$
    $(u, v) \leftarrow (u^+, v^+)$
end
```

$$P_\eta(\xi)_{i,p} = \frac{\xi_{i,p}}{\max\left(1, \frac{\|\xi\|_F}{\eta}\right)} \quad \text{and} \quad P^1_{L_2}(\xi) = \frac{\xi}{1 + \frac{\tau}{\lambda}} \quad \text{and} \quad P^2_{L_2}(\xi) = \frac{\tau\delta u_{i,j} + \eta_i}{1 + \tau\delta}$$

Bibliography

[1] O. Dössel, *Bildgebende Verfahren in der Medizin.* Springer, 2000. Von der Technik zur medizinischen Anwendung.

[2] S. C. Deoni, B. K. Rutt, and T. M. Peters, "Rapid combined T1 and T2 mapping using gradient recalled acquisition in the steady state," *Magnetic Resonance in Medicine*, vol. 49, no. 3, pp. 515–526, 2003.

[3] N. Stikov, M. Boudreau, I. R. Levesque, C. L. Tardif, J. K. Barral, and G. B. Pike, "On the accuracy of T1 mapping: Searching for common ground," *Magnetic Resonance in Medicine*, vol. 73, no. 2, pp. 514–522, 2015.

[4] L. I. Sacolick, F. Wiesinger, I. Hancu, and M. W. Vogel, "B1 mapping by Bloch-Siegert shift," *Magnetic Resonance in Medicine*, vol. 63, no. 5, pp. 1315–1322, 2010.

[5] L.-C. Chang, C. G. Koay, P. J. Basser, and C. Pierpaoli, "Linear least-squares method for unbiased estimation of T1 from SPGR signals," *Magnetic Resonance in Medicine*, vol. 60, no. 2, pp. 496–501, 2008.

[6] K. T. Block, M. Ücker, and J. Frahm, "Model-Based Iterative Reconstruction for Radial Fast Spin-Echo MRI," *IEEE Transactions on Medical Imaging*, vol. 28, pp. 1759–1769, Nov 2009.

[7] J. A. Fessler, "Model-Based Image Reconstruction for MRI," *IEEE Signal Processing*

Magazine, vol. 27, pp. 81–89, July 2010.

[8] T. J. Sumpf, M. Ücker, S. Boretius, and J. Frahm, "Model-based nonlinear inverse reconstruction for T2 mapping using highly undersampled spin-echo MRI," *Journal of Magnetic Resonance Imaging*, vol. 34, no. 2, pp. 420–428, 2011.

[9] V. Roeloffs, X. Wang, T. J. Sumpf, M. Untenberger, D. Voit, and J. Frahm, "Model-based reconstruction for t1 mapping using single-shot inversion-recovery radial flash," *Int. J. Imaging Systems and Technology*, vol. 26, pp. 254–263, 2016.

[10] C. M. Lewis, S. A. Hurley, M. E. Meyerand, and C. G. Koay, "Data-driven optimized flip angle selection for T1 estimation from spoiled gradient echo acquisitions," *Magnetic Resonance in Medicine*, vol. 76, no. 3, pp. 792–802, 2016.

[11] H.-L. M. Cheng and G. A. Wright, "Rapid high-resolution T1 mapping by variable flip angles: Accurate and precise measurements in the presence of radiofrequency field inhomogeneity," *Magnetic Resonance in Medicine*, vol. 55, no. 3, pp. 566–574, 2006.

[12] S. C. Deoni, T. M. Peters, and B. K. Rutt, "Determination of optimal angles for variable nutation proton magnetic spin-lattice, T1, and spin-spin, T2, relaxation times measurement," *Magnetic Resonance in Medicine*, vol. 51, no. 1, pp. 194–199, 2004.

[13] T. Hilbert, D. Nguyen, J.-P. Thiran, G. Krueger, T. Kober, and O. Bieri, "trueflash: Model-based iterative t1 mapping using variable-flip-angle fast low-angle shot," *Proc. Intl. Soc. Mag. Reson. Med. 24*, 2016.

[14] D. Ma, V. Gulani, N. Seiberlich, K. Liu, J. L Sunshine, J. Duerk, and M. Griswold, "Magnetic resonance fingerprinting," *Nature*, vol. 495, pp. 187–92, 03 2013.

[15] S. E. Russek, E. F. Jackson, D. L. Jennings, J. L. Evelhoch, J. L. Gunter,

and A. G. Sorensen, "Characterization of NIST/ISMRM MRI System Phantom. Poster presented at the ISMRM 20^{th} Annual Meeting and Exhibition," 2012. url: https://collaborate.nist.gov/mriphantoms/bin/view/MriPhantoms/MRISystemPhantom.

[16] F. Liu, J. V. Velikina, W. F. Block, R. Kijowski, and A. A. Samsonov, "Fast realistic MRI simulations based on generalized multi-pool exchange tissue model," *IEEE Transactions on Medical Imaging*, vol. 36, pp. 527–537, Feb 2017.

[17] O. Maier, J. Schoormans, M. Schlögl, G. J. Strijkers, A. Lesch, T. Benkert, T. Block, B. F. Coolen, K. Bredies, and R. Stollberger, "Rapid T1 quantification from high resolution 3D data with model-based reconstruction," *Magnetic Resonance in Medicine*, vol. 81, no. 3, pp. 2072–2089, 2019.

[18] K. Bredies, K. Kunisch, and T. Pock, "Total Generalized Variation," *SIAM Journal on Imaging Sciences*, vol. 3, no. 3, pp. 492–526, 2010.

[19] F. Knoll, K. Bredies, T. Pock, and R. Stollberger, "Second order total generalized variation (TGV) for MRI," *Magnetic Resonance in Medicine*, vol. 65, no. 2, pp. 480–491, 2011.

[20] K. Bredies and M. Holler, "A TGV-Based Framework for Variational Image Decompression, Zooming, and Reconstruction. Part I: Analytics," *SIAM Journal on Imaging Sciences*, vol. 8, no. 4, pp. 2814–2850, 2015.

[21] A. Chambolle and T. Pock, "A first-order primal-dual algorithm for convex problems with applications to imaging," *Journal of mathematical imaging and vision*, vol. 40, no. 1, pp. 120–145, 2011.

[22] T. Pock, D. Cremers, H. Bischof, and A. Chambolle, "Global Solutions of Variational Models with Convex Regularization," *SIAM J. Imaging Sciences*, vol. 3, pp. 1122–1145, 2010.

[23] M. Holler and K. Kunisch, “On Infimal Convolution of TV-Type Functionals and Applications to Video and Image Reconstruction,” *SIAM Journal on Imaging Sciences*, vol. 7, no. 4, pp. 2258–2300, 2014.

[24] M. Schlögl, M. Holler, A. Schwarzl, K. Bredies, and R. Stollberger, “Infimal convolution of total generalized variation functionals for dynamic mri,” *Magnetic Resonance in Medicine*, vol. 78, no. 1, pp. 142–155, 2017.

[25] M. Schlögl, M. Holler, O. Maier, T. Benkert, K. Bredies, K. T. Block, and R. Stollberger, “Highly Accelerated Quantitative MRI with ICTGV Regularized Reconstruction.,” *Proc. Intl. Soc. Mag. Reson. Med. 25*, 2017.

[26] A. B. Kerr, C. H. Cunningham, J. M. Pauly, J. E. Piel, R. O. Giaquinto, R. D. Watkins, and Y. Zhu, “Accelerated B1 mapping for parallel excitation.,” *Proceedings of the 15th Annual Meeting of ISMRM p 352*, 2007.

[27] C. H. Cunningham, J. M. Pauly, and K. S. Nayak, “Saturated double-angle method for rapid B1+ mapping,” *Magnetic Resonance in Medicine*, vol. 55, no. 6, pp. 1326–1333, 2006.

[28] N. G. Dowell and P. S. Tofts, “Fast, accurate, and precise mapping of the rf field in vivo using the 180Âř signal null,” *Magnetic Resonance in Medicine*, vol. 58, no. 3, pp. 622–630, 2007.

[29] M. Ücker, T. Hohage, K. T. Block, and J. Frahm, “Image reconstruction by regularized nonlinear inversion - Joint estimation of coil sensitivities and image content,” *Magnetic Resonance in Medicine*, vol. 60, no. 3, pp. 674–682, 2008.

[30] M. Ücker, S. Zhang, and J. Frahm, “Nonlinear inverse reconstruction for real-time MRI of the human heart using undersampled radial FLASH,” *Magnetic Resonance in Medicine*, vol. 63, no. 6, pp. 1456–1462, 2010.

[31] X. Wang, V. B. Roeloffs, K. D. Merboldt, D. Voit, S. Schätz, and J. Frahm, "Single-shot multi-slice T1 mapping at high spatial resolution - Inversion-recovery FLASH with radial undersampling and iterative reconstruction," *The Open Medical Imaging Journal*, vol. 9, pp. 1–8, 2015.

[32] S. Winkelmann, T. Schaeffter, T. Koehler, H. Eggers, and O. Dössel, "An optimal radial profile order based on the golden ratio for time-resolved MRI," *IEEE transactions on medical imaging*, vol. 26 1, pp. 68–76, 2007.

[33] T. Block, H. C.Handarana, and S. Milla, "Towards routine clinical use of radial stack-of-stars 3D gradient-echo sequences for reducing motion sensitivity," *JKorean Soc Magn Reson Med*, vol. 18, pp. 87–106, 01 2014.

[34] R. Heule, C. Ganter, and O. Bieri, "Variable flip angle T1 mapping in the human brain with reduced T2 sensitivity using fast radiofrequency-spoiled gradient echo imaging," *Magnetic Resonance in Medicine*, vol. 75, no. 4, pp. 1413–1422, 2016.

[35] C. Lin, M. Bernstein, J. Huston, and S. Fain, "Measurements of T1 relaxation times at 3.0T: Implications for clinical MRA," *Proc. Intl. Soc. Mag. Reson. Med. 9*, 2009.

[36] J. Imran, F. Langevin, and H. Saint-Jalmes, "Two-point method for T1 estimation with optimized gradient-echo sequence.," *Magnetic resonance imaging*, vol. 17 9, pp. 1347–56, 1999.

[37] B. J. Jellison, A. S. Field, J. Medow, M. Lazar, M. S. Salamat, and A. L. Alexander, "Diffusion tensor imaging of cerebral white matter: A pictorial review of physics, fiber tract anatomy, and tumor imaging patterns.," *AJNR. American journal of neuroradiology*, vol. 25, pp. 356–369, Mar. 2004.

[38] L. Zhi-Pei and E. Haacke, "Magnetic resonance imaging," *Biomedical Imaging V - Proceedings of the 5th IEEE EMBS International Summer School on Biomedical Imaging, SSBI 2002*, 1 2002.

[39] G. Ramos-Llordén, G. Vegas-Sánchez-Ferrero, M. Björk, F. Vanhevel, P. M. Parizel, R. San José Estépar, A. J. den Dekker, and J. Sijbers, "NOVIFAST: A fast algorithm for accurate and precise VFA MRI T1 mapping," *IEEE Transactions on Medical Imaging*, vol. 37, pp. 2414–2427, Nov 2018.